united nations educational, scientific and cultural organization

international atomic energy agency

the
abdus salam
international centre for theoretical physics

SMR/1108 - 16

COURSE ON "MEDITERRANEAN SEA(S) CIRCULATION & ECOSYSTEM FUNCTIONING" 2 - 20 November 1998

Trieste, Italy

"Residual and Gravity Currents in the Gulf of California"

J. OCHOA DE LA TORRE
CICESE
Ensenasda, Mexico

JOURNAL OF GEOPHYSICAL RESEARCH, VOL. 102, NO. C4, PAGES 8611–8623, APRIL 15, 1997

Tidal residual currents in the Gulf of California: Is the M_2 tidal constituent sufficient to induce them?

S. G. Marinone
Departamento de Oceanografía Física, Centro de Investigación Científica y de Educación Superior de Ensenada. Ensenada. México

Abstract. A two-dimensional vertically integrated numerical model has been used to study residual, that is, mean and low-frequency (< 0.5 cycles per day) currents, in the Gulf of California. The model is forced at the mouth with the most important tidal constituents. allowing them to interact through the nonlinear terms. Previous nonlinear models of the gulf were forced only with the most energetic M_2 constituent. The mean residual currents obtained with the semidiurnal constituents are all of the same order (1-2 cm s^{-1}) as those obtained with the M_2 alone and are larger by an order of magnitude than those produced by the diurnal components. The time-mean residual obtained with all seven constituents is very close to that obtained with only the M_2. When several constituents are included simultaneously, fluctuating residuals arise in the model through nonlinear interactions. The fortnightly variation produced by the interaction of M_2 and S_2 constituents is the most important, and it is of the same order of magnitude as the time-mean residual. The model shows that time-averaged residuals can effectively be computed from the M_2 component alone, whereas the fluctuating residual, which is equally important, requires the inclusion of the S_2 constituent as well. Thus computations with only the M_2 and S_2 constituents yield a very good approximation for computing tidally induced residual currents in the Gulf of California.

1. Introduction

The Gulf of California (Figure 1a) is a marginal sea between mainland México and the Baja California peninsula. It is roughly 150 km wide and 1100 km long and has a maximum depth of 3600 m at its connection with the Pacific Ocean to the south.

The tides in the Gulf of California have been recorded and studied for several years. A complete description of the different tidal constituents is given by *Morales and Gutiérrez* [1989]. A generally observed and modeled feature of the tides in the gulf is the amplification that all constituents experience toward the head, both by resonance (the wavelength of the semidiurnal constituents makes the gulf a quarter-wave oscillator) and by shoaling of the bottom [*Hendershott and Speranza*, 1971; *Filloux*, 1973; R. Dressler. unpublished manuscript, 1981]. Among the semidiurnal constituents, the resonant conditions in the shallow northern basin cause an amplitude close to 2 m for the M_2 component alone, whereas the total tide reaches an amplitude of nearly 5 m [*Bray and Robles*, 1991].

The Gulf of California has a long modeling history. One-, two- and three-dimensional models have been used to study the tides. The most popular have been the two-dimensional (2-D) models, both linear [e.g., *Grijalva*, 1972; *Stock*, 1976] and nonlinear [*Quirós et al.*, 1992, *Carbajal*, 1993; *Argote et al.*, 1995; R. Dressler, unpublished manuscript, 1981]. The nonlinear models have used only the M_2 constituent to represent the tidal phenomena of the gulf. R. Dressler (unpublished manuscript, 1981) modeled the different constituents individually, and *Carbajal* [1993] forced the model with several tidal constituents simultaneously but did not calculate any residuals.

Time-averaged residual currents from the M_2 constituent alone in the Gulf of California have been computed by *Durazo* [1989], *Quirós et al.* [1992], *Carbajal* [1993], and M. L. Argote et al. (manuscript in preparation, 1996). When full nonlinear interaction is allowed and several constituents are included, a low-frequency response is produced as well [*Marinone et al.*, 1996]; thus residual current is defined here as that part of the flow left after low-pass filtering the currents with a cutoff period of 2 days. It consists of a mean (time averaged) and a fluctuating (deviation from the mean) component.

The seven most important constituents in the Gulf of California show a large amplification from the mouth of the gulf to its head (Table 1). The M_2 has the largest amplitude, but the rest of the constituents are also important. From this, the following questions arise: (1) Are the mean residual currents induced by the different constituents important? (2) Are the mean residual currents induced by the nonlinear interaction of all con-

Paper number 96JC03835.
0148-0227/97/96JC-03835$09.00

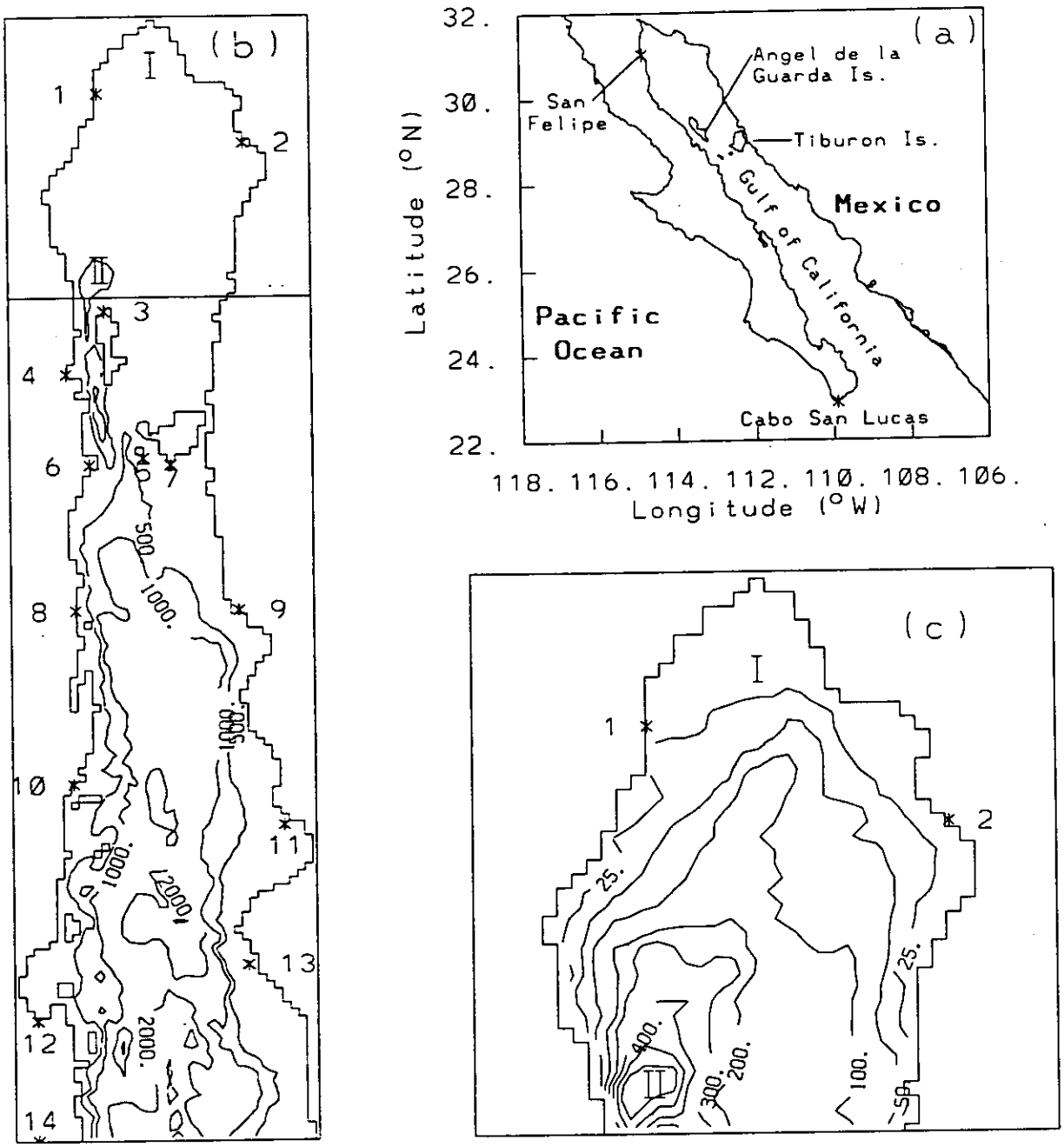

Figure 1. (a) Plan view of the Gulf of California. (b) Horizontal layout of the two-dimensional model. Numbers 1-14 are tidal station locations used to calibrate the model (see Table 3). (c) Amplification with bathymetry in meters of the area where most of the results are shown.

stituents different than those produced only by the M_2? (3) Is the low-frequency component of the residual important?

Here the tidally induced residual currents in the Gulf of California are studied with a 2-D vertically integrated model forced by tides. The residuals are generated only by interactions of tides and topography, and the study focuses on the generation of residuals from the different diurnal and semidiurnal tidal constituents, as well as from their nonlinear interactions.

2. The Model

We use the depth-averaged model developed by *Crean* [1978], which has been used extensively and successfully reproduces the observed tidal heights and currents in several places (e.g., Juan de Fuca/Georgia Strait system [*Crean et al.*, 1988]). A full description of the model is given by *Crean et al.* [1988].

The equations used in the model are

Table 1. Major Tidal Constituents at Cabo San Lucas and San Felipe

Constituent	Period	Cabo San Lucas Amplitude	San Felipe Amplitude
M_2	12.42	36.8	164.5
S_2	12.00	23.7	99.3
N_2	12.66	8.8	42.0
K_2	11.97	6.6	26.4
K_1	23.93	22.2	41.6
O_1	25.82	15.2	26.3
P_1	24.07	6.9	13.0

Periods are given in hours and amplitudes in centimeters. See Figure 1 for their locations.

$$\frac{\partial U}{\partial t}+\frac{\partial}{\partial x}\left(\frac{U^2}{d}\right)+\frac{\partial}{\partial y}\left(\frac{UV}{d}\right)-fV+gd\frac{\partial \eta}{\partial x}+\tau_x-\nu\nabla^2 U=0,$$

$$\frac{\partial V}{\partial t}+\frac{\partial}{\partial x}\left(\frac{UV}{d}\right)+\frac{\partial}{\partial y}\left(\frac{V^2}{d}\right)+fU+gd\frac{\partial \eta}{\partial y}+\tau_y-\nu\nabla^2 V=0,$$

$$\frac{\partial \eta}{\partial t}+\nabla\cdot(\vec{v}d)=0,$$

where the bottom stresses are given by a quadratic law, namely,

$$\vec{\tau}=(\tau_x,\tau_y)=\frac{C_d\sqrt{U^2+V^2}}{d^2}\vec{V},$$

and $f=2\Omega\sin(\varphi)$ is the Coriolis parameter, $\vec{V}$ is the transport vector with components U and V, $\vec{v}$ is the velocity vector with components u and v, which are related to the transport components as $(u,v)=(U,V)/d$, $d=\eta+h$ is the total depth, η and h are the surface elevation and bottom depth with respect to the mean sea level. g is the acceleration due to gravity, C_d is the bottom friction coefficient, and ν is the eddy viscosity coefficient ($=10^2$ m^{2}s^{-1}).

The model equations are solved explicitly from rest, and the tidal elevations were specified at the open boundary at all times from observed tidal harmonics. The chosen model time step, Δt, was 22.5 s, which satisfies the Courant-Friedrichs-Lewy criterion [*Courant et al.*, 1928] with a mesh size of 6.48 × 6.48 km. Figure 1 shows the gulf discretization and bathymetry.

Several runs were performed forcing the model with only the M_2 tidal component and with all seven tidal constituents and varying the coefficient of friction C_d until the best agreement with the observed tidal harmonics at several tidal stations around the gulf was obtained. This happened for $C_d=4.4\times10^{-3}$ with the multiple tidal forcing. The results are qualitatively consistent with those obtained by *Argote et al.* [1995], who used $C_d=3.7\times10^{-3}$ (and the same ν). Significant differences among runs are obtained only if C_d is varied by more than 30%. The residual currents of these runs were also verified, and in this range of C_d, the spatial structure of the currents is preserved and their magnitude increases as C_d decreases. For example, for $C_d=0.002$, the rms of the residual currents is 0.83 cm s^{-1}, while for $C_d=0.006$, the rms is 0.38 cm s^{-1}.

After calibration, the following runs were designed. First, four runs with a single forcing constituent, namely, M_2, S_2, K_1, and O_1, were performed. Second, two runs combining two forcing constituents each, namely, M_2, S_2 and K_1, O_1, were performed. Finally, two additional runs were performed, one with four and the other with all seven forcing constituents. Table 2 lists the different runs with their corresponding forcing constituents and labels. One anticipates that the interactions between these tides will give rise to oscillations in the model at frequencies which are the sums and differences of the forcing frequencies. Therefore the runs are long enough to ensure that we capture most of the model's low-frequency fluctuations and that a stable mean can be computed. The lengths of the simulations were 14 days for runs M2, S2, K1, and O1; 56 days for runs SD and D; a half year for run main; and 1 year for run all. (The Raleigh's criterion [*Otnes and Enochson*, 1972] gives, for example, a period of 182 days for the K_2-S_2 interaction. Harmonic analysis of a 1-year model run resolves this modulation well.)

3. Results

3.1. The Tides

The distribution of amplitudes and phases of the constituents modeled in runs M2, S2, K1, and O1 are almost identical to those obtained from the multiple forced runs (SD, D, main or all). Figure 2 shows amplitudes and phases throughout the gulf from run all; the results are very similar to those observed by *Morales and Gutiérrez* [1989]. Tables 3, 4, and 5 show the modeled and observed amplitudes and phases at several stations around the gulf for the M_2, S_2, and K_1 constituents, respectively; their differences are minimal.

The agreement with observations (and with the modeled M_2 by *Argote et al.* [1995]) is considered satisfactory. *Argote et al.* [1995; manuscript in preparation, 1996] have compared model results with observations; as the results obtained here are almost identical to theirs, no additional comparisons with observations will be shown.

Table 2. Forcing Constituents Included in the Different Model Runs

Run	M_2	S_2	K_1	O_1	P_1	N_2	K_2
M2	X						
S2		X					
K1			X				
O1				X			
SD	X	X					
D			X	X			
Main	X	X	X	X			
All	X	X	X	X	X	X	X

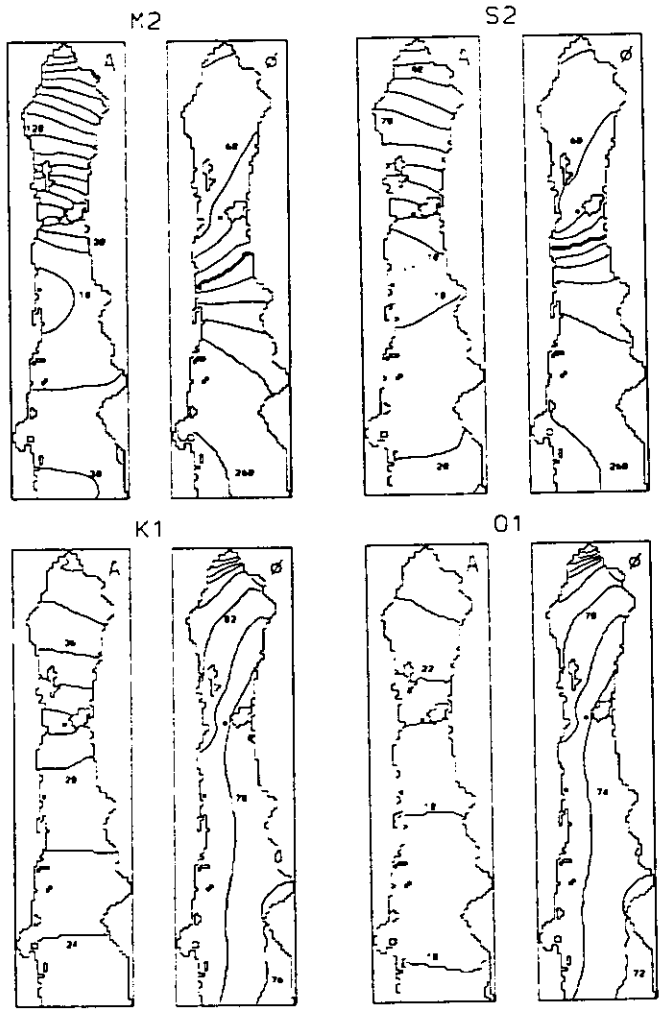

Figure 2. Modeled amplitude. A (centimeters), and phase, ϕ (degrees with respect to Greenwich), in the Gulf of California for the M_2. S_2. K_1, and O_1 tidal constituents. A and o contour increments for the semidiurnal constituents are 10 cms and 20° and for the diurnal constituents are 2 cm and 2°. Thick lines for the phases of the M_2 and S_2 constituents corresponds to 360°.

3.2. The Residual Circulation

3.2.1. Time-averaged residual. The residual currents are very small in the south and central gulf and large around the islands and in the northern part of the gulf; in the rest of the paper the results will focus on the northern part. Figure 3 shows the time-averaged currents for the single semidiurnal constituent forced runs. The numbers in the figure (upper left corner of each panel) are the rms of the speed in the area shown, which is largest in Figure 3a. The largest model residuals are produced by the M_2, but all semidiurnal constituents produce currents of similar magnitude (Figure 4d). The residuals associated to the diurnal constituents (Figure 4b) are an order of magnitude smaller. Run M2 (Figure 3a) is very similar to that reported by M. L. Argote et al. (manuscript in preparation, 1996). The spatial structure of the residual flow of the different cases is about the same. If we were to simply add all the residuals produced by the different tidal constituents independently, a quite large residual would result compared to run all (as will be shown below).

Figure 4 shows the mean residual currents forced by the multiple tidal constituents. Figures 4a and 4b correspond to the forcing by two constituents, two semidiurnal and two diurnal, each. Figures 4c and 4d show the cases of four and seven tidal constituents, respectively. The run with only two diurnal constituents (K_1 and O_1) is the most different and the one with the smallest velocities. The other three runs, SD, main, and all, are very similar to each other. The structure of the flow when the semidiurnal constituents are included is very similar because the contribution to the mean from the diurnal constituents is minimal. The flow, generally, follows the isobaths, and the largest velocities are found where bottom slopes are largest. The largest currents were produced by run all.

The differences among these runs can best be appreciated from Figure 5, where the differences of some runs with run all, chosen as the reference run, are shown.

Table 3. Amplitudes and Phases Observed (A_{obs} and ϕ_{obs}) and Modeled (A_{mod} and ϕ_{mod}) for the M_2 Constituent in the Gulf of California

	Station	A_{obs}	ϕ_{obs}	A_{mod}	ϕ_{mod}	δA	$\delta\phi$
1	San Felipe	164.5	64.9	174.0	76.5	9.5	11.6
2	Puerto Peñasco	157.0	58.6	163.0	65.3	6.0	6.7
3	Puerto Refugio	100.6	59.1	108.0	66.8	7.4	7.7
4	Bahía de Los Angeles	65.6	58.7	73.2	67.8	7.6	9.1
5	Isla Esteban	36.7	43.7	40.6	50.8	3.9	7.1
6	San Francisquito	42.4	56.2	40.8	64.9	-1.6	8.7
7	Isla Tiburón	36.5	24.4	37.6	39.5	1.1	15.1
8	Santa Rosalía	9.2	354.1	6.8	4.7	-2.4	10.6
9	Guaymas	13.5	315.8	11.9	324.0	-1.6	8.2
10	Loreto	14.5	275.8	13.5	271.0	-1.0	-4.8
11	Yavaros	20.4	296.3	19.6	283.0	-0.8	-13.3
12	La Paz	23.7	274.9	26.5	269.0	2.8	-5.9
13	Topolobampo	29.3	297.9	24.5	259.0	-4.8	-38.9
14	San Lucas	36.8	252.5	36.8	252.5	0.0	0.0
	Standard deviation					4.4	14.1

Amplitudes are given in centimeters and phases are given in degress with respect to greenwich. Differences between modeled and observed values (δA and δo) are given.

Table 4. Amplitudes and Phases Observed (A_{obs} and ϕ_{obs}) and Modeled (A_{mod} and ϕ_{mod}) for the S_2 Constituent in the Gulf of California

	Station	A_{obs}	ϕ_{obs}	A_{mod}	ϕ_{mod}	δA	$\delta\phi$
1	San Felipe	99.2	64.6	95.5	76.4	-3.8	11.8
2	Puerto Peñasco	93.9	59.0	89.3	64.1	-4.6	5.1
3	Puerto Refugio	56.4	59.8	57.3	64.8	0.9	5.0
4	Bahía de Los Angeles	35.0	58.8	37.3	64.9	2.2	6.1
5	Isla Esteban	18.6	34.7	19.2	42.4	0.6	7.7
6	San Francisquito	19.2	52.0	18.7	59.3	-0.5	7.3
7	Isla Tiburón	18.0	11.6	18.0	28.1	0.0	16.5
8	Santa Rosalía	5.4	303.5	5.5	304.0	0.1	0.5
9	Guaymas	10.7	289.2	9.9	297.0	-0.8	7.8
10	Loreto	12.6	264.8	12.2	266.0	-0.4	1.2
11	Yavaros	15.6	287.2	15.5	275.0	-0.1	-12.2
12	La Paz	17.9	272.0	19.1	265.0	1.2	-7.0
13	Topolobampo	20.9	294.5	18.1	259.0	-2.8	-35.5
14	San Lucas	23.7	252.0	23.7	252.0	0.0	0.0
	Standard deviation					1.9	12.8

Amplitudes are given in centimeters and phases are given in degress with respect to greenwich. Differences between modeled and observed values (δA and $\delta\phi$) are given.

It is clear that as long as the forcing includes the M_2 (i.e., runs M2, SD, main), the time-averaged currents do not differ much. The rms speed is small compared to the runs that exclude the semidiurnal constituents; that is, it is enough to force the model with only the M_2 to compute time-averaged currents. Run S2 and a run with only the N_2 tidal component (not shown) each produced residual currents comparable to Run M2. When all constituents are included simultaneously, the mean does not change much, indicating that not all the additional energy is transferred to the mean residual but goes to high and low frequencies (that is, compound tides and overtides) and, as will be shown later, more energy is dissipated by friction as well.

3.2.2. Time-dependent fluctuations. Motions with periods of less than approximately 2 days were removed by passing the fields three times through a 25-hour running average filter, which passes about 50% of the amplitude at 0.3 cycles per day and 95% of the amplitude at 0.08 cycles per day while reducing the semidiurnal and diurnal amplitudes to less than 1% of their original values [*Yao et al.*, 1982].

Figure 6 shows a series of snapshots of the fluctuating residual, with mean removed. The amplitudes of these currents are close to those of the mean velocities. Fluctuations are dominated by a 14-day cycle (compare days 7 and 21), essentially by the Msf tidal constituent. Spectral analyses (not shown) indicate that most of the energy at low frequencies is in the beat frequencies of the M_2, S_2, and N_2 constituents, the Msf from the M_2-S_2 components, the Mm from the M_2-N_2 components, and at the beat frequency of the N_2-S_2 constituents. These low frequencies arise by nonlinear interactions in the model, as they are absent in the forcing.

Table 5. Amplitudes and Phases Observed (A_{obs} and ϕ_{obs}) and Modeled (A_{mod} and ϕ_{mod}) for the K_1 Constituent in the Gulf of California

	Station	A_{obs}	ϕ_{obs}	A_{mod}	ϕ_{mod}	δA	$\delta\phi$
1	San Felipe	41.6	82.0	39.4	86.3	-2.2	4.3
2	Puerto Peñasco	43.4	79.4	38.8	80.9	-4.6	1.5
3	Puerto Refugio	36.8	79.9	35.5	81.4	-1.3	1.5
4	Bahía de Los Angeles	33.8	80.1	32.9	81.7	-0.9	1.6
5	Isla Esteban	31.9	78.2	30.4	78.4	-1.5	0.2
6	San Francisquito	34.6	79.6	30.4	81.4	-4.2	1.8
7	Isla Tiburón	30.6	77.7	30.0	76.6	-0.6	-1.1
8	Santa Rosalía	28.9	79.9	27.4	79.4	-1.5	-0.5
9	Guaymas	28.0	75.7	26.9	77.1	-1.1	1.4
10	Loreto	26.3	79.0	25.7	79.7	-0.6	0.7
11	Yavaros	25.4	76.2	25.5	76.3	0.1	0.1
12	La Paz	25.0	84.1	24.0	76.0	-1.0	-8.1
11	Topolobampo	25.3	87.2	24.2	79.8	-1.1	-7.4
14	San Lucas	22.2	78.9	22.1	78.9	0.0	0.0
	Standard deviation					1.4	3.4

Amplitudes are given in centimeters and phases are given in degress with respect to greenwich. Differences between modeled and observed values (δA and $\delta\phi$) are given.

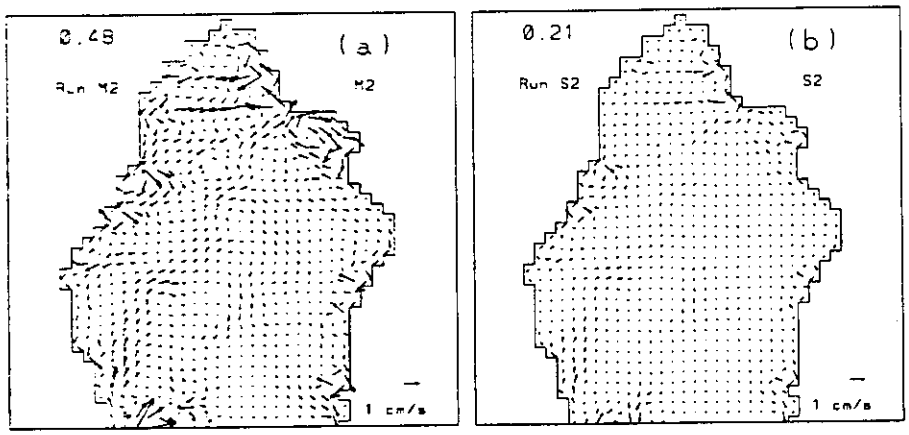

Figure 3. Time-averaged currents (centimeters per second) for the runs forced by the (a) M_2 (run M2) and (b) S_2 (run S2). The numbers in the upper left corners are the rms of the speeds (in centimeters per second) for the area shown.

Figure 7 shows the amplitudes of the indicated low-frequency constituents for the v field. (The amplitudes are very similar for the u component and are not shown.) The dominant mode is the Msf, followed by the Mm, N_2-S_2, and Ssa constituents. The latter appears in the model through the interaction of the K_2-S_2 constituents and the generated Msf-Mf constituents.

Comparison of the fluctuating residual obtained with run all and those of the other runs shows that it is enough to force the model with the M_2 and S_2 con-

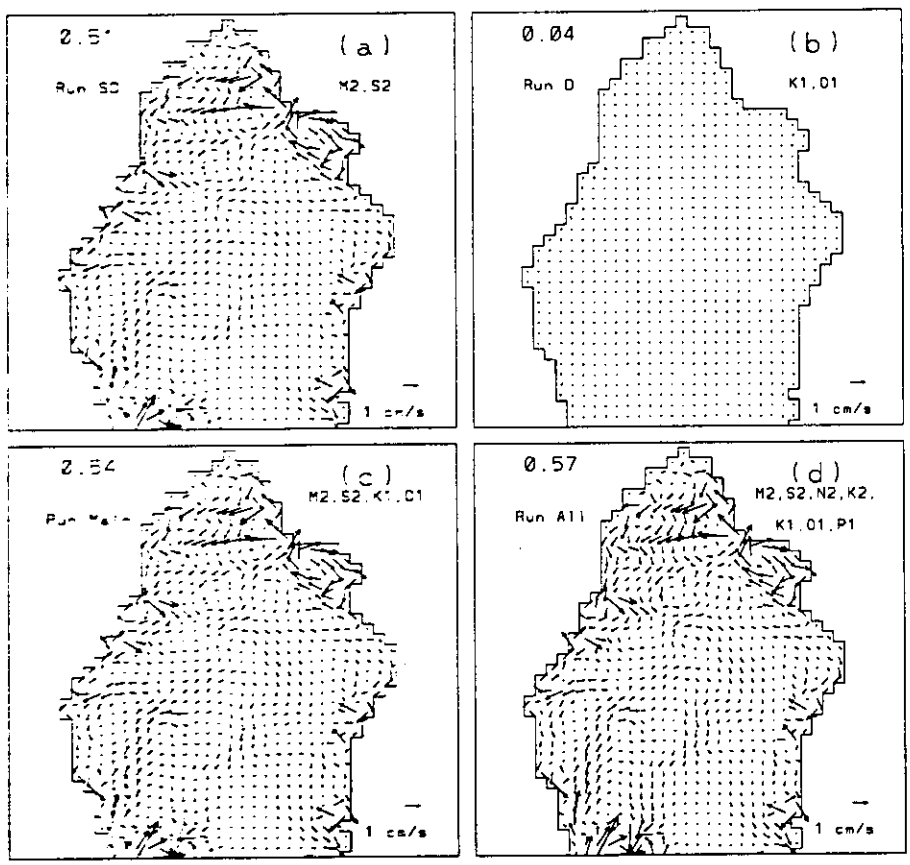

Figure 4. Time-averaged currents (centimeters per second) for the runs forced by the (a) M_2 and S_2 (run SD), (b) K_1 and O_1 (run D), (c) M_2, S_2, K_1, and O_1 (run main), and (d) M_2, S_2, N_2, K_2, K_1, O_1, and P_1 (run all) tidal constituents. The numbers in the upper left corners are the rms of the speeds (in centimeters per second) for the area shown.

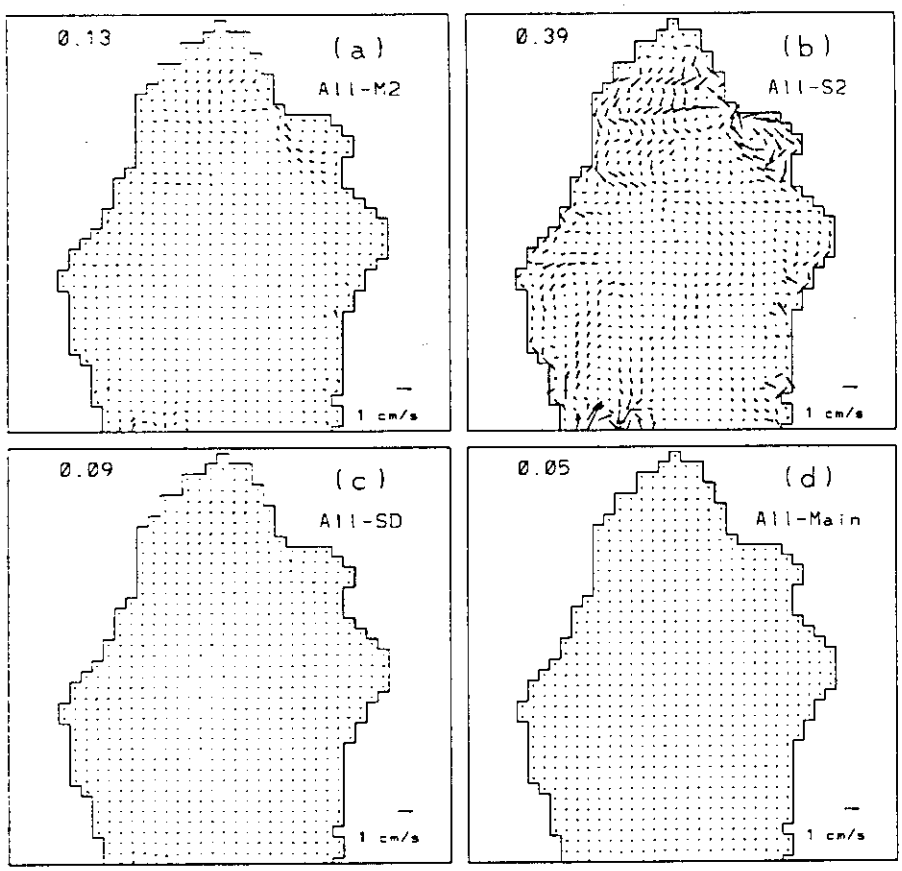

Figure 5. Difference of the time-averaged currents (centimeters per second) between run all and the runs forced by the (a) M_2 (run M2), (b) S_2 (run S2), (c) M_2 and S_2 (run SD) and (d) M_2, S_2, K_1, and O_1 (run main) tidal constituents. The numbers in the upper left corners are the rms of the speeds (in centimeters per second) for the area shown.

stituents to induce this component of the residual; run all and run SD fluctuating residuals are almost identical.

3.3. Diagnostic Calculations

3.3.1. Momentum. It is well known that tidal residual currents appear as a result of a rectification process as the tides interact with topography [*Zimmerman*, 1978]. *Huthnance* [1973] showed that the Coriolis force and bottom drag are the mechanisms responsible for the generation of residuals, while the role of the advective terms is to transfer properties (e.g., vorticity) from the tides to the mean field [*Zimmerman*, 1980; *Robinson*, 1983].

In the Gulf of California, friction plays an important role, especially in the northern part where it is shallow (see *Argote et al.* [1995] for different estimates of tidal dissipation). Here all the terms of the momentum equations are evaluated from the model results in order to identify the main balances that generate or maintain the residual currents in the gulf. The terms of the equations were evaluated from the total fields, low-pass filtered (as with the u and v fields), and time averaged.

The spatial variability of the balances is large for both the fluctuating and mean residuals (the horizontal eddy viscosity terms are negligible). Figure 8 shows a time series of the terms in the x and y momentum equations at points I and II, which are shown in Figure 1c. No single dominant balance is evident. Pressure gradients are always part of the main balance. For point I, in the x equation, Coriolis and pressure gradient forces are balanced by friction and advection, while, in the y equation, the presure gradient alone is balanced by friction and advection. At point II, where depth is larger, there is almost a geostrophic balance, with advection playing a role in both the x and y equations.

Figures 9 and 10 show the dominant terms in the time-mean x and y equations throughout the northern gulf. In some deep areas, where all the terms are small, the dominant balance is close to geostrophic (especially in the x equation, Figure 9), with advection playing a smaller role. In shallow areas, all the terms are larger with the exception of the Coriolis force, which remains small, that is, pressure gradients are balanced by friction and advection. The dominant pressure gradient term is linked to the correlation between the pressure

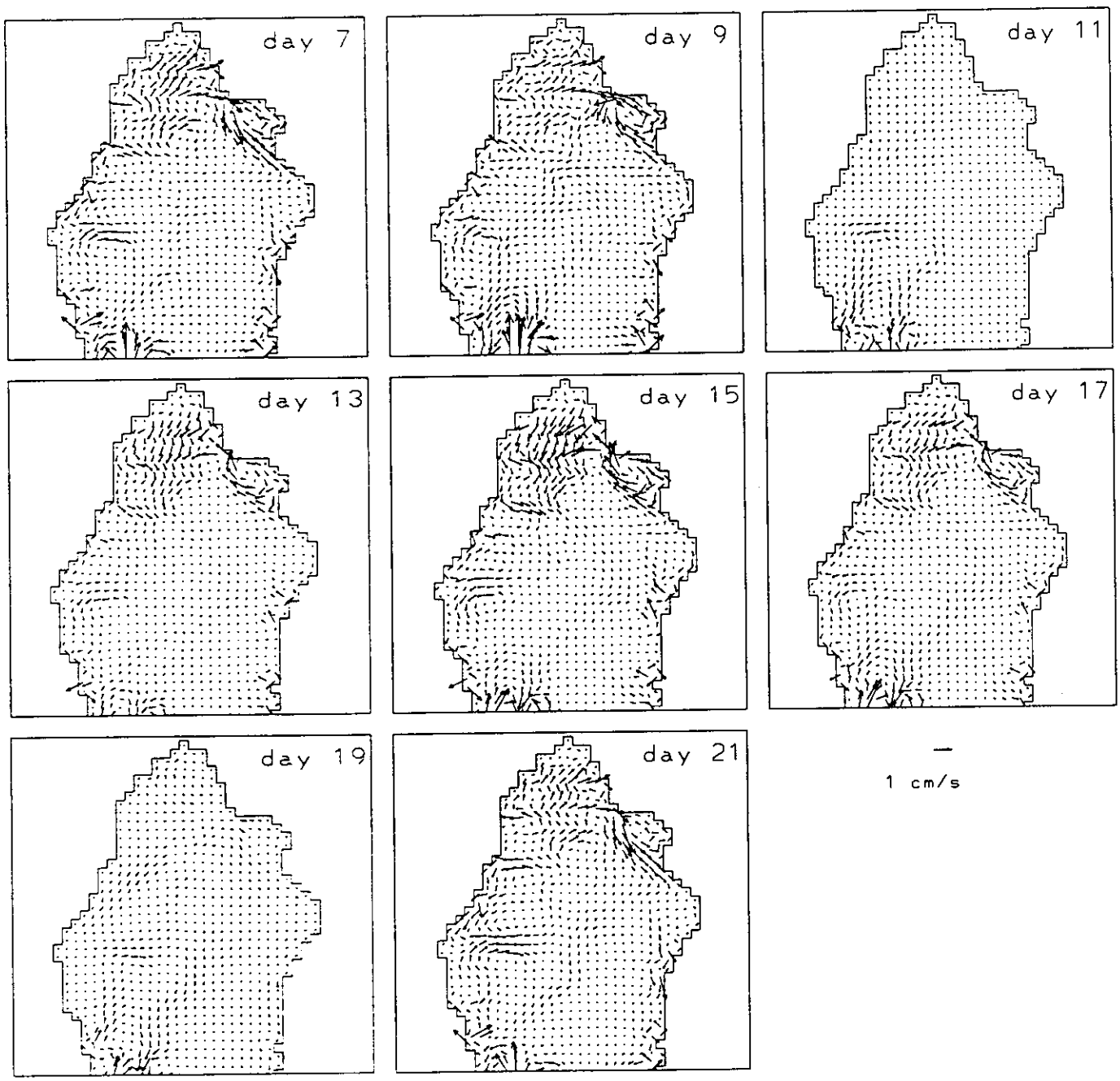

Figure 6. Snapshots of the fluctuating residual at 2-day intervals for run all.

field and the bottom topography [*Haidvogel and Brink*, 1986]. The frictional spin-down times (of the order of 2-5 hours) are small compared to the inertial period in the northern extremity of the gulf. The modeled residuals are larger in these shallow areas.

Thus, in agreement with tidal rectification theories [e.g., *Huthnance*, 1973; *Loder*, 1980], residuals in the Gulf of California result mainly from bottom drag, advection, and Earth rotation; also, the strongest currents are found where the tidal excursions (3-5 km) are similar to the topographic length scale ($h/\nabla h$).

3.3.2. Energetics. In section 3.2.1 it was shown that the sum of the residual currents produced by the M_2 and S_2 single forcing constituents gives larger residuals than when both constituents are run together. The inclusion of more energy into the system, by means of additional tidal constituents, in a nonlinear system is such that part of the net energy flux is transferred to the mean flow, another part is transferred to the fluctuations, but most of it is lost by frictional dissipation. Here we calculate the energy dissipation and the different terms of the mechanical energy equation derived from the original equations of motion, namely,

$$\frac{\partial E}{\partial t} = -D - \nabla \cdot \vec{Q},$$

where $E = \frac{1}{2}[(u^2+v^2)(\eta+h)+g\eta^2]$ is the sum of kinetic

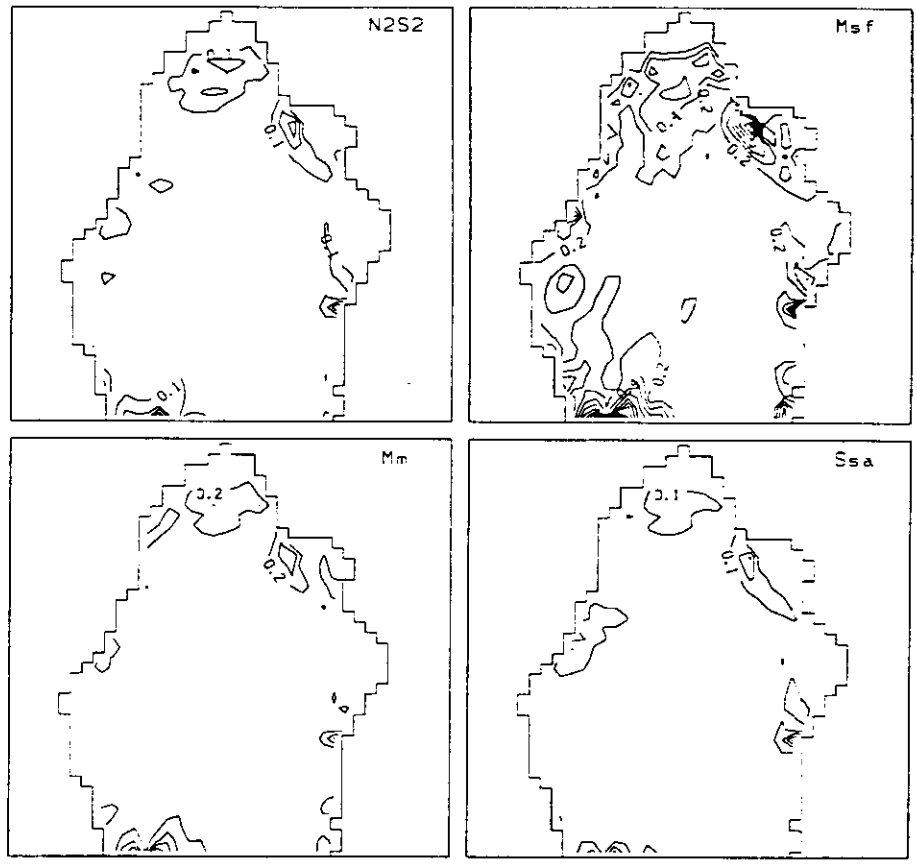

Figure 7. Amplitudes of the v component of velocity (in centimeters per second) for the indicated low-frequency tidal constituents.

and potential energy, $D = C_d(u^2 + v^2)^{\frac{3}{2}}$ is the energy dissipation rate, and $\vec{Q} = \vec{v}(\eta + h)[(u^2 + v^2)/2 + g\eta]$ is the energy flux. Integrating over the modeled region,

$$\frac{\partial}{\partial t}(\quad) = -\langle D \rangle - \langle F \rangle$$

where $\langle \ldots \rangle = \int \ldots dA$. The flux at the open boundary is $F = \vec{Q} \cdot \hat{n} dS$, where $\hat{n}$ is a unit normal vector and ds is an element length along the boundary. Values of the different terms were computed for each mesh point according to the model discretization. (To estimate the rate of change of total energy in the system, and as a check of these diagnostic calculations, we (1) numerically differentiated the signal $E(t)$ every hour from the hourly model output and between successive time steps and (2) took the difference between the open boundary flux and frictional dissipation (energy loss by viscosity was also included). The agreement between the three calculations is excellent, the different plots being almost indistinguishable from each other.)

Figure 11 shows time series of $\langle E \rangle$, $\langle D \rangle$, and $\langle F \rangle$ for different runs. In Figure 11a the total energy is shown; it is largest for run all and then decreases as tidal constituents are excluded. From the single forcing constituent runs, the M_2 case has, obviously, the largest energy level and the diurnal cases the lowest (not shown). The largest terms of the energy equation are $\langle D \rangle$ and $\langle F \rangle$, which almost balance each other (the difference is accounted for by the eddy dissipation term and the rate of change of energy).

Table 6 shows the time-averaged values of the terms shown in Figure 11 (the averages correspond to the whole length of the different runs, which are different among runs) and the root mean squared values of the mean residual speeds in the northern part of the Gulf of California. Again, the magnitude of the terms increases as more tidal constituents are included; however, the combination of the single forcing constituents cases does not add up to that of the run that includes the above combination. For example, $\langle D \rangle_{M2} + \langle D \rangle_{S2} < \langle D \rangle_{SD}$, where the subindices label the different runs; that is, there is more dissipation (and also more energy flux) in the multiple-constituent forcing runs. (The friction coefficient is the same for the different runs; also, *Pingree* [1983] showed that a quadratic friction law may not be strictly valid, as assumed here, when both constituents, the M_2 and S_2 are run together.) The value of $\langle D \rangle$ for the M_2 is 3.14×10^9W, *Argote et al.* [1995] es-

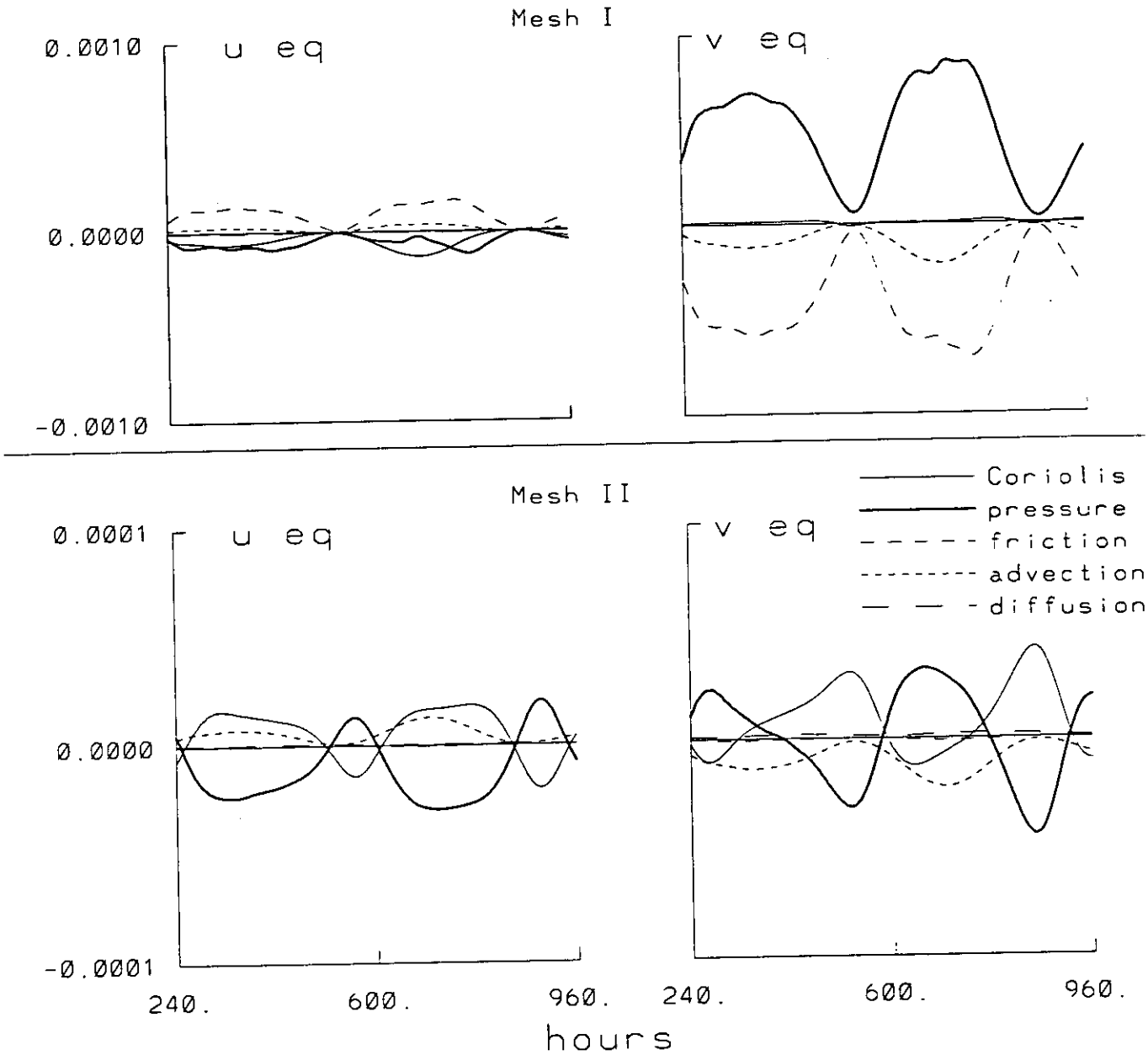

Figure 8. Budget analysis of the x and y momentum equations, in cm s^{-2}, for two mesh points (see Figure 1c for their location).

timated a dissipation of energy for the same constituent of 3.92 × 10^9 W. *Ripa and Velázquez* [1993] estimated a dissipation rate, with a linear model, of 8.5 and 2.9 × 10^9 W for the M_2 and S_2, respectively. The S_2 energy dissipation is about a third of the M_2; in this work, the ratio is smaller (0.2).

The time-averaged total energy level $\langle E \rangle$ has lower levels when the constituents are forcing the model simultaneously, $\langle E \rangle_{M2} + \langle E \rangle_{S2} > \langle E \rangle_{SD}$; in the same way, as we noted in the beginning of this section, the sum of the residual currents by the individual runs results in a larger residual than when they are included simultaneously, a fact reflected in the rms values, $\mathrm{rms}_{M2} + \mathrm{rms}_{S2} > \mathrm{rms}_{SD}$.

Running the model with multiple constituents has important consequences that should not be overlooked. Energy is being transferred to low-frequency fluctuations (as well as to high ones, which we include in the mean) which cannot be represented when only one constituent is used.

Finally, $\langle D \rangle$ should be equal to $\langle F \rangle$, but the agreement (see Table 6) is considered reasonable in view of the approximations of the finite difference form of the energy equation. For example, frictional dissipation at a point was computed using velocities at four grid points, whereas the frictional terms in the original equations involved velocities from 12 grid points [*Crean et al.*, 1988]. Also, part of the difference is due to eddy viscosity loss.

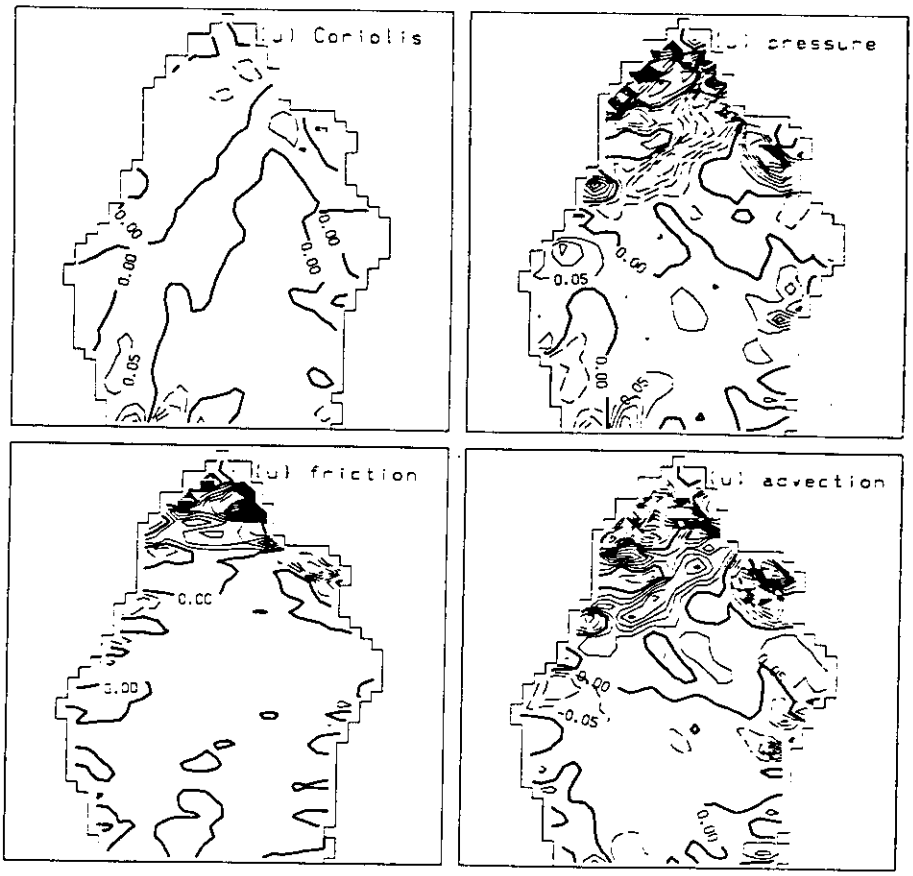

Figure 9. Main time-averaged forces of the u momentum equation. The terms are normalized such that the largest absolute value taken across all terms and in all the gulf is unity. Contour interval is 0.05, solid lines are positive values, and dashed lines are negative values.

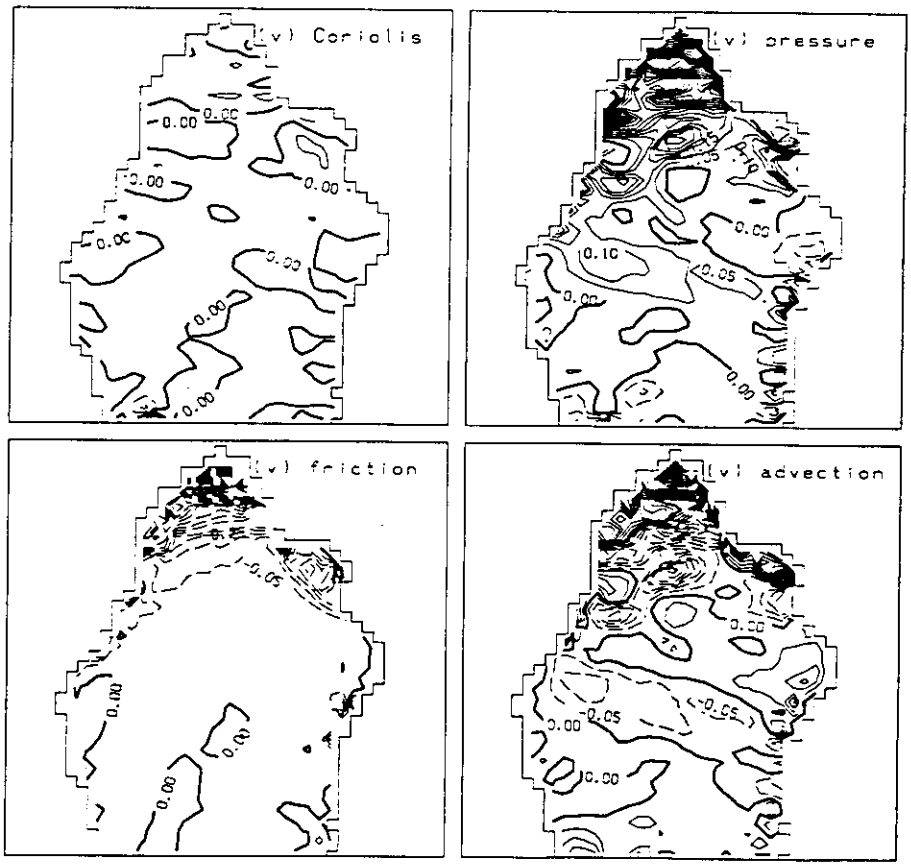

Figure 10. Main time-averaged forces of the v momentum equation. The terms are normalized such that the largest absolute value taken across all terms and in all the gulf is unity. Contour interval is 0.05, solid lines are positive values, and dashed lines are negative values.

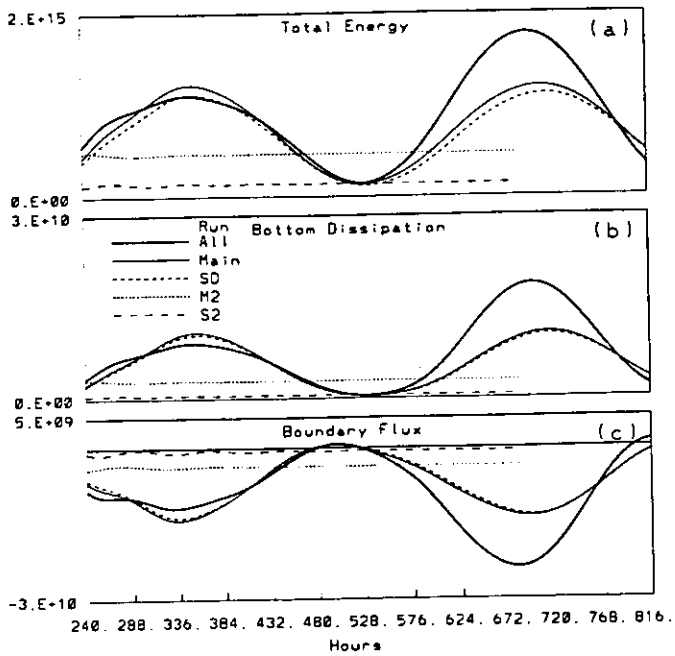

Figure 11. Time series of the (a) total energy $\langle E \rangle$, (b) energy dissipation by bottom friction $\langle D \rangle$ and (c) energy flux at the boundary $\langle F \rangle$, for runs M2, S2, SD, main, and all (see Table 2).

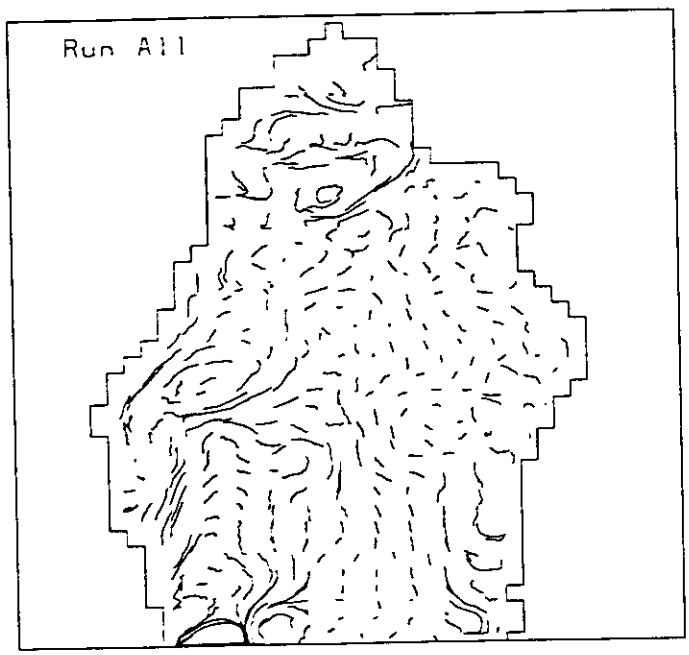

Figure 12. Trajectories followed by "particles" advected by the flow field of tidal currents produced by the tidal components M_2, S_2, N_2, K_2, K_1, O_1, and P_1. The oscillatory part due to tides (diurnal and higher frequencies) has been removed.

4. Summary

Tidal residual currents in the Gulf of California are basically generated by the semidiurnal components. Answering the questions of section 1, the M_2 (mainly) and S_2 are the main tidal constituents producing mean residual currents, and their interaction feeds, basically, all the energy that is being transferred to low frequencies. Both, the time mean and the fluctuating residuals are of the same order of magnitude with velocities around 2 cm s^{-1} in the northern part of the gulf.

The dynamics of the residual currents is highly nonlinear. It was found that friction and advection are chiefly responsible for producing the residuals in shallow areas, whereas, in deeper areas the main balance is geostrophic. The energy calculations also reflect this nonlinear behavior; the energy dissipation is larger when both tidal components are run together than the linear sum of the individual contributions.

Table 6. Energetics of the Different Runs

Run	$\langle E \rangle$	$\langle D \rangle$	$\langle F \rangle$	rms
M2	5.00×10^{14}	3.13×10^{9}	3.45×10^{9}	0.48
S2	1.55×10^{14}	6.00×10^{8}	6.89×10^{8}	0.21
SD	6.17×10^{14}	4.90×10^{9}	5.23×10^{9}	0.51
Main	6.79×10^{14}	5.07×10^{9}	5.34×10^{9}	0.54
All	7.31×10^{14}	5.74×10^{9}	6.00×10^{9}	0.57

Values correspond to the time averages of the model domain integral of the total energy, $\langle E \rangle$ (Joules), energy dissipation by bottom friction, $\langle D \rangle$ (Watts), energy flux at the open boundary, $\langle F \rangle$ (Watts), and the corresponding rms of the speeds (centimeters per second) for the northern gulf.

The residual currents reported here are certainly small; however, they can contribute more to the overall long-term distribution and transport of properties than do, for example stronger, but intermittent and directionally variable wind-driven flows [*Robinson*, 1983].

The fact that the residual currents produced only by the M_2 tidal constituent do not differ much from the multiple forced runs does not mean that the total currents are the same. The total currents from the multiple constituents runs are larger and show all the typical time variability of the observed tides (mixed tides, fortnightly tides, etc.). Figure 12 shows the low-pass filtered particle trajectories driven by the multiple constituent total flow field (run all). These trajectories are almost identical to the ones obtained with only the M_2 constituent (run M2). Therefore, even though the total flow is very different, the residual currents and the net displacement of particles are about the same.

Acknowledgments. This research was financed by Centro de Investigación Científica y de Educación Superior de Ensenada, Baja California, México. The tidal harmonics were provided by Cuauhtemoc Nava and Ignacio González and the bathymetry by Alberto Amador. I thank two anonymous reviewers for helpful comments and Antoine Badan, Miguel Lavín, P. Ripa, and F. J. Ocampo Torres for critically reading the manuscript.

References

Argote, M.L., A. Amador, M. F. Lavín, and J.R. Hunter, Tidal dissipation and stratification in the Gulf of California, *J. Geophys. Res.*, *100*, 16,103-16.118, 1995.

Bray, N.A., and J. M. Robles, Physical oceanography of the Gulf of California, in *The Gulf of California and Peninsular Provinces of the Californias*, edited by J.P. Dauphin and B.R. Simoneit, *AAPG Mem., 47*, 511-553, 1991.

Carbajal, N., Modelling of the circulation in the Gulf of California, Ph.D. thesis, 186 pp., Univ. of Hamburg, Hamburg, Germany, 1993.

Courant, R., K. Friedrichs, and H. Lewy, Uber die partiellen differenzengleichungen der mathemathischen physik, *Math. Ann., 100*, 32-74, 1928.

Crean, P., A numerical model of barotropic mixed tides between Vancouver Island and the mainland and its relation to studies of the estuarine circulation, in *Hydrodynamics of Estuaries and Fjords*, edited by J. Nihoul, pp. 283-314, Elsevier, New York, 1978.

Crean, P., T. Murty, and J. Stronach, *Mathematical Modeling of Tides and Estuarine Circulation, Coastal Estuarine Stud.*, Vol. 30, 471 pp., AGU, Washington, D.C., 1988.

Durazo, R., Frentes térmicos de verano en al alto Golfo de California, M.S. thesis, 66 pp., Cent. de Invest. Cient. y Educ. Super. de Ensenada, Ensenada, México, 1989.

Filloux, J.H., Tidal patterns and energy balance in the Gulf of California: Observations from a spaceborne radar, *Nature, 243*, 217-221, 1973.

Grijalva, N., Tidal computation in the Gulf of California, *Geofis. Int., 12*, 13-34, 1972.

Haidvogel, D. B., and K. H. Brink, Mean currents driven by topographic drag over the continental shelf and slope, *J. Phys. Oceanogr., 16*, 2159-2171, 1986.

Hendershott, M.C., and A. Speranza, Co-oscillating tides in long narrow bays; the Taylor problem revisited, *Deep Sea Res., 18*, 959-980, 1971.

Huthnance, J. M., Tidal asymmetries over the Norfolk Sandbanks, *Estuarine Coastal Mar. Sci., 1*, 89-99, 1973.

Loder, J. W., Topographic rectification of tidal currents on the sides of Georges Bank, *J. Phys. Oceanogr., 10*, 1399-1416, 1980.

Marinone, S. G., S. Pond, and J. Fyfe, A three-dimensional model of tide and wind induced residual currents in the central Strait of Georgia, B. C., *Estuarine Coastal Shelf Sci., 43*, 157-182, 1996.

Morales, R.A., and G. Gutiérrez, Mareas en el Golfo de California, *Geofis. Int., 28*, 25-46, 1989.

Otnes, R. K., and L. Enochson, *Digital time series analysis*, 467 pp., John Wiley, New York, 1972.

Pingree, R.D., Spring tides and quadratic friction, *Deep Sea Res., Part A, 30*, 929-944, 1983.

Quirós, G., A. Badan-Dangon, and P. Ripa, M_2 currents and residual flow in the Gulf of California, *Neth. J. Sea Res., 28*, 251-259, 1992.

Ripa, P., and G. Velázquez, Modelo unidimensional de la marea en el Golfo de California, *Geofis. Int., 32*, 41-56, 1993.

Robinson, I. S., Tidally induced residual flows, in *Physical Oceanography of Coastal and Shelf Seas*, edited by B. Johns, pp. 321-356, Elsevier, New York, 1983.

Stock, G.G., Modeling tides and dissipation in the Gulf of California, Ph.D. thesis, 102 pp., Scripps Inst. of Oceanogr., Univ. of Calif., San Diego, La Jolla, 1976.

Yao, T., S. Pond and L. A. Mysak, Low-frequency subsurface current and density fluctuations in the Strait of Georgia, *Atmos. Ocean, 20*, 340-356, 1982.

Zimmerman, J. T. F., Topographic generation of residual circulation by oscillatory (tidal) current, *Geophys. Astrophys. Fluid Dyn., 11*, 35-47, 1978.

Zimmerman, J. T. F., Vorticity transfer by tidal currents over an irregular topography, *J. Mar. Res., 38*, 601-630, 1980.

S. G. Marinone, Departamento de Oceanografía Física, Centro de Investigación Científica y de Educación Superior de Ensenada, P.O. Box 434844, San Diego, CA 92143-4844. (e-mail: marinone@cicese.mx)

(Received December 12, 1995; revised October 15, 1996; accepted October 29, 1996.)

Estuarine, Coastal and Shelf Science (1998), 47, 000–000
Article No. ec980387

Inverse-estuarine Features of the Upper Gulf of California

M. F. Lavín, V. M. Godínez and L. G. Alvarez

Departamento de Oceanografía Física, CICESE, Ensenada, Baja California, México

Received 14 April 1998 and accepted in revised form ??? 1998

The Upper Gulf of California is the shallow (depth <30 m), tidal area at the head of the Gulf of California. It is an inverse estuary, due to the high evaporation rate ($E \sim 1{\cdot}1$ m year) and almost nil freshwater input from rainfall and the Colorado River. Historical and recent hydrographic data show that the area is almost vertically well-mixed throughout the year, that the horizontal distribution of properties follows the bathymetry, and that the hydrography has a strong annual modulation. As in other negative estuaries, the year-round salinity increase toward the head causes the density to do likewise, despite the seasonally reversing temperature gradient. The pressure gradient thus formed leads to water-mass formation and gravity currents (speed $\sim 0{\cdot}1$ ms^{-1}), both in winter and in summer. In winter, the high salinity water sinks beyond 200 m, while in summer it only reaches a depth of 20–30 m. The gravity currents appear to be modulated by the fortnightly tidal cycle, with events in neap tides. This phenomenon causes the presence, at least during neap tides, of slight stratification ($\Delta\sigma_t \approx -0{\cdot}2$).

Keywords: inverse estuaries; gravity currents; warm semi-enclosed seas; Mexico coast

Introduction

The Upper Gulf of California (Figure 1), henceforth abbreviated UGC, is the shallow northernmost part of the Gulf of California. It has a triangular shape, bound by the 30 m isobath and the coverging coast of mainland México and the Baja California Peninsula. It is a highly tidal sea, with maximum spring tidal amplitude of about 5 m, and tidal current speeds exceeding 1 ms^{-1} (Alvarez Sánchez *et al.*, 1993). It now enjoys a Biosphere Reserve status, for it is the home of indigenous endangered species (*Totoaba macdonaldi* or Totoaba, and *Phocoena sinus* or Vaquita), as well as a zone of reproduction and nursery ground for many others, including some of economical importance. The management of the resources of the UGC will be hampered by a lack of basic knowledge about the physical environment. The little that is known about the oceanography of the UGC by direct observation is based in hydrographic data collected almost monthly between October 1972 and September 1973 (Alvarez-Borrego *et al.*, 1973). This is what is known, from those observations, at present:

(1) Surface temperature increases to the NW in summer and decreases in winter. Temperature maxima (~ 32 °C) are attained in August, and minima (~ 8 °C) in December (Alvarez-Borrego & Galindo-Bect, 1974; Alvarez-Borrego *et al.*, 1975).
(2) Surface salinity always increases to the NW, with a seasonal maximum (39) in May-September and minimum (37) in December-February (ibid).
(3) The UGC is vertically well-mixed throughout the year (Organista Sandoval, 1986; Martínez Sepúlveda, 1994).
(4) The front between the vertically well-mixed regime of the UGC and stratified conditions is found about the 30 m isobath in summer, and that of ~ 60 m in winter (Argote *et al.*, 1995).

Features (1) and (2) can readily be observed in Figure 2. Based on the pattern of the surface distributions of salinity and temperature, a cylonic residual circulation has been proposed for the UGC (Alvarez-Borrego & Galindo-Bect, 1974). Only the surface distributions were described by Alvarez-Borrego and Galindo-Bect (1974) and Alvarez-Borrego *et al.* (1975). Indeed not even the distribution of surface density has been described, and Figure 2 shows the so-far unnoticed (and very interesting) fact that density increases toward the NW both in winter and summer.

By numerical modelling, the following has been proposed:

(1) Tidal mixing is responsible for maintaining the summer-time well-mixed conditions of the UGC, and therefore controls the summer position of the mixing front. In winter, vertical convection is added to tidal

0272-7714/98/000000+00 $30.00/0

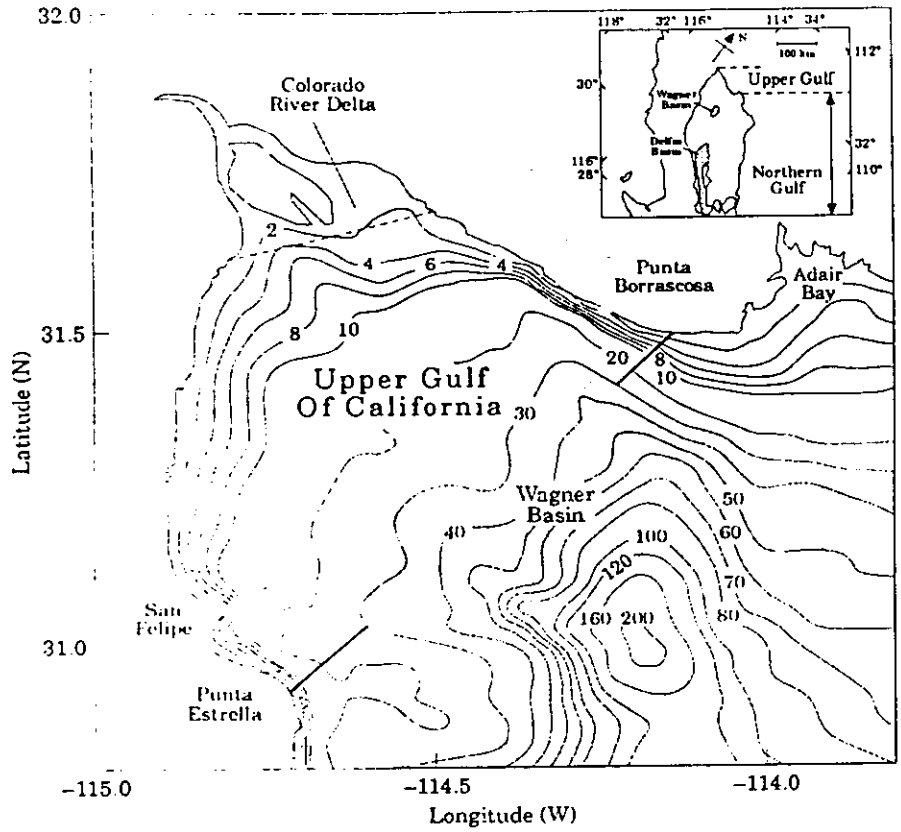

FIGURE 1. Bathymetry of the Upper Gulf of California (UGC), taken here as the area with bottom depth less than 30 m, to the NW of a line between Punta Estrella and Punta Borrascosa. Depth in metres.

mixing in controlling the front location (Argote *et al.*, 1995).

(2) The predicted circulation in the UGC due to topographic tidal rectification is different for different models. According to Argote *et al.* (1998) there is a convergence at the Delta, and a southward compensating jet along the axis. Marinone (1997) finds a cyclonic circulation. Carbajal *et al.* (1997) do not obtain a well-defined circulation. In all cases the residual speeds are of O (0·01 ms^{-1}). These numerical results are very sensitive to the bathymetry, to the grid resolution and to the friction coefficient; also they are very difficult to verify by observation.

(3) The wind, which blows from the NW in winter and from the SE in summer, induces a cyclonic residual circulation in winter and an anticyclonic circulation in summer, of O (0·02–0·03 ms^{-1}) (Carbajal, 1993; Beier, 1997; Argote *et al.*, 1998). No data are available to support any of these numerical results for the UGC, although they agree with observations made just south of the UGC, in Delfin Basin (Lavín *et al.*, 1997; Argote *et al.*, 1998).

In this paper historical and recent hydrographic data are used to make an updated description of the hydrography of the UGC, including vertical structure and its seasonal variability. Water mass formation is also discussed and observations of gravity currents shown.

Observations

The study area

The bathymetry on the peninsular side has a gently sloping bottom and, in the mean, is shallower than the mainland side, where the bottom depth rapidly reaches the maximum of the cross-section, in a channel or canyon that extends to the 200 m-deep Wagner Basin. The natural southern limit of the UGC is the front separating the vertically well-mixed coastal waters of the UGC and the stratified waters of Wagner Basin. As mentioned before, the 30 m isobath marks the approximate summer position of that front, and therefore is a convenient sea-boundary or limit of the UGC.

Historical data

The historical data were collected approximately monthly between October 1972 and September 1973;

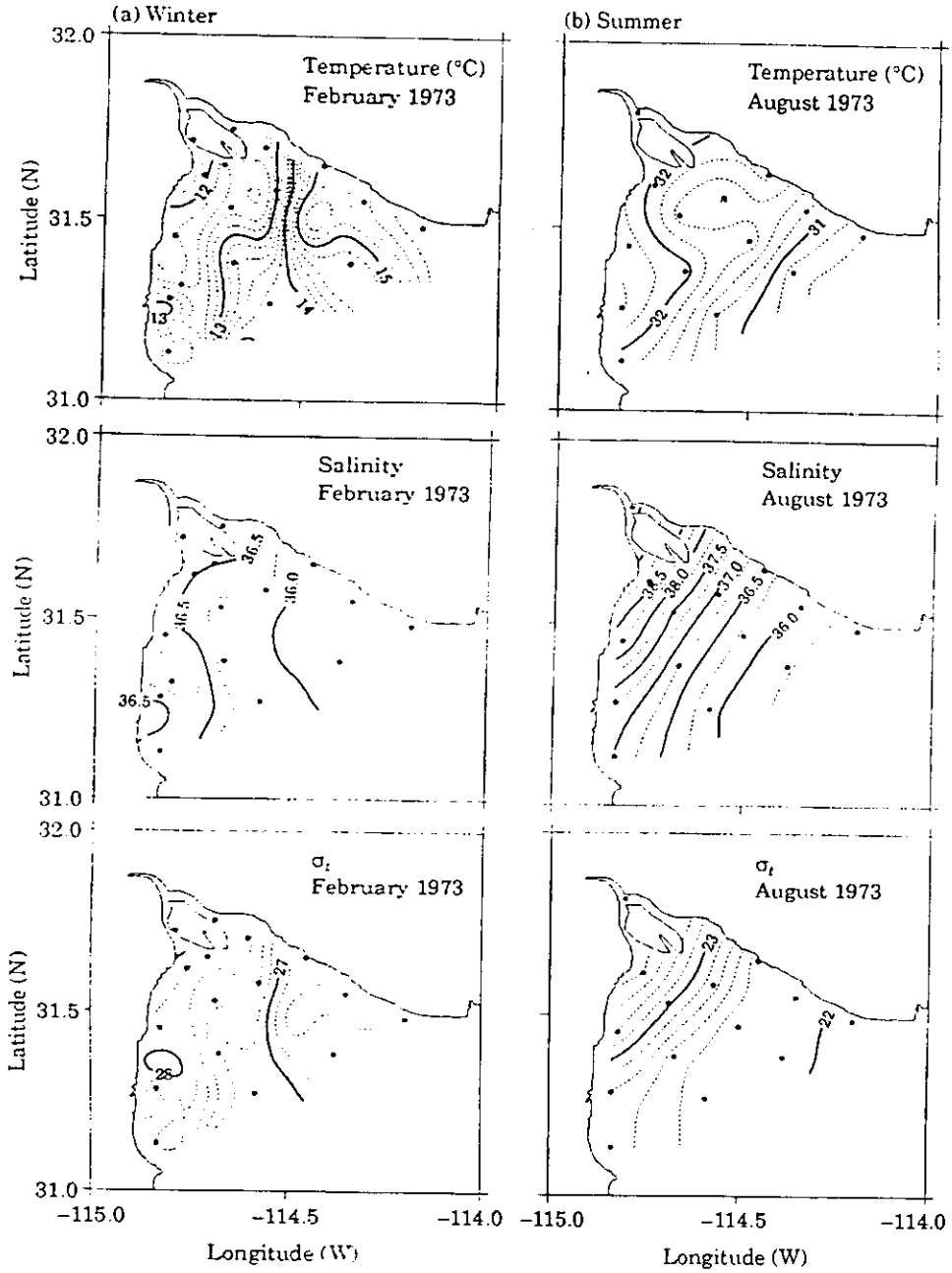

FIGURE 2. Surface distribution of temperature, salinity and sigma-t from the historical data. Two examples are shown: (a) winter (February 1973) and (b) summer (August 1973).

typical station coverage is shown by the dots in Figure 2, and Figure 3(*a*) shows the position of all the stations. The October 1972 data are not used here because of unusual rainy conditions; the full set of data can be found in the report by Alvarez-Borrego *et al.* (1973). Although this is the only data set available and covers a full annual period, it has some limitations. The data were collected with bottles and reversing thermometers only at 0, 5 and 10 m; therefore the bottom layer was not sampled in a very wide area where the bottom depth exceeds 10 m (see Figure 1). The station separation is quite large, with only three across-gulf rows of four stations each in the main body of the UGC.

New data

CTD data were obtained in the UGC on seven separate occasions between December 1993 and July

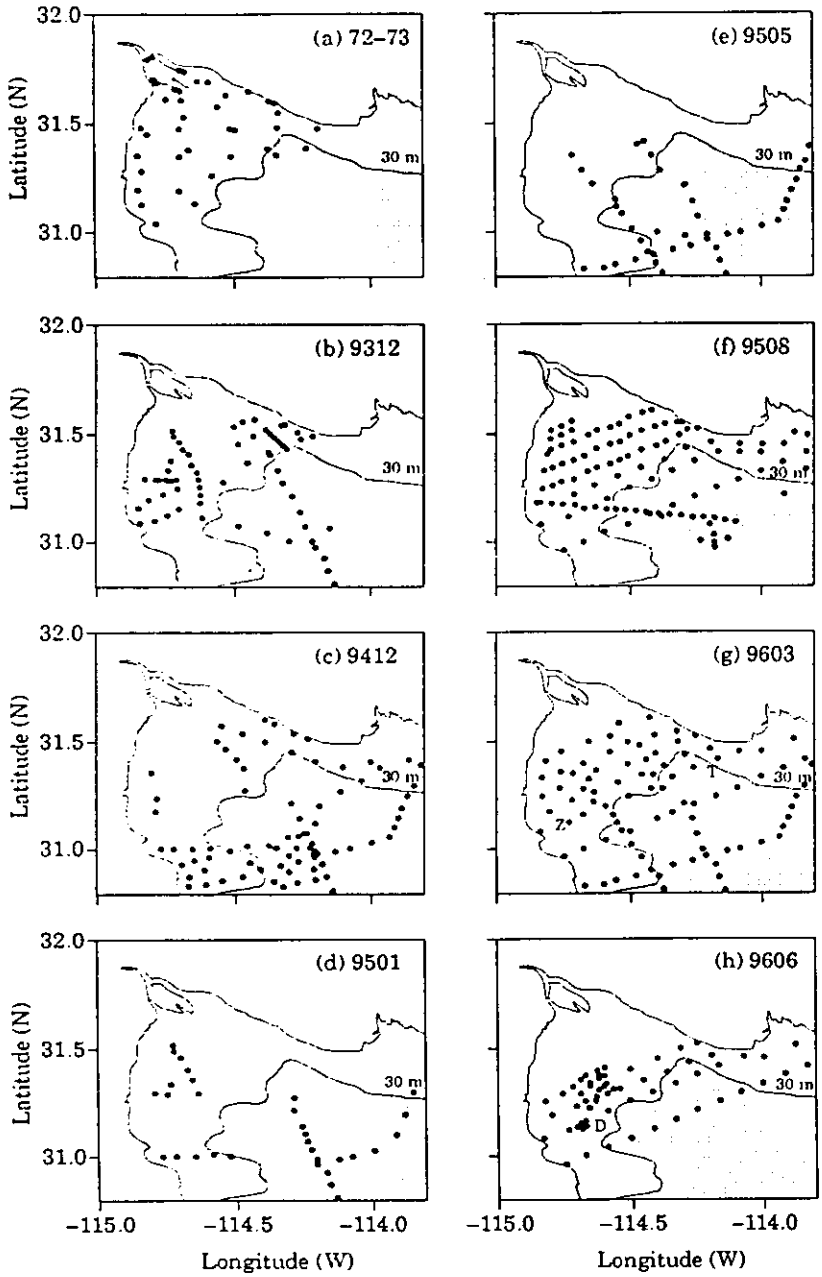

FIGURE 3. (a) Positions of the stations of the historical data. (b) to (h) Positions of the CTD stations made between December 1993 and June 1996. The surveys are named according to the year and month when they took place (e.g. 9606=June 1996). The sites of time-series measurements are marked as follows: in 9603 (g), the current meter mooring sites are marked by Z and T. In 9606 (h), the current meters were moored at site D, two CTD time series were also made at site D, one at spring and one at neap tides.

1996, always from the BO *Francisco de Ulloa*. The station separation [Figure 3(b)–(h)] is smaller than in the historical data, but full coverage of the UGC was not always achieved; in fact, no data were collected in the Delta. Some of the across-UGC lines of stations intersect the deeper-than-30 m channel in the mainland side, and it will be seen that stratified conditions are almost always encountered there, with clear near-bottom intrusions of water from Wagner Basin. The data from the best sampled surveys will be presented in some detail, in a constructed annual cycle. The full data set, including the points in Figure 3 that fall outside the UGC, will be used in the T/S diagram. All the CTD surveys were made in neap tides, so that the vessel could venture as far north as it did.

TABLE 1. Details of current meter installations in the Upper Gulf of California during March and June 1996

Site	Lat. (°N)	Long. (°W)	Bottom depth (m)	CM height (m)	δt (min) ΔT (days)	START (hh:mm dd/m/yy)	END (hh:mm dd/m/yy)	S/N
Z	31 08·24	114 40·38	22	5	20 3·76	17:40 26/3/96	12:00 29/3/96	AA 11653
T	31 24·11	114 11·48	25	5	20 14·66	00:00 26/3/96	16:00 09/4/96	GO 489
D Neaps	31 08·25	114 40·38	22	1	10 2·54	19:30 23/6/96	08:40 26/6/96	AA 11653
D Neaps	31 08·25	114 40·38	22	6	10 2·52	19:50 23/6/96	08:30 26/6/96	GO 489
D Springs	31 08·25	114 40·38	22	1	10 4·07	06:20 28/6/96	08:10 01/7/96	AA 11653
D Springs	31 08·25	114 40·38	22	6	10 3·98	07:00 28/6/96	06:40 01/7/96	GO 489

The sampling rate is δt (minutes), and the length of the time series is ΔT (days). GO, General Oceanics; AA, Aanderaa.

In the survey made in December 1993 (coded as 9312), a Neil-Brown Smart CTD was used; its field and laboratory calibrations are reported by Godinez *et al.* (1995). In all the other surveys a factory-calibrated SBE-911*plus* CTD was used, and the data were processed using the manufacturer's software, as detailed by Garcia *et al.* (1995); data interpolated to 2 m intervals are used here. The current meters used were either Aanderaa RCM-7 or General Oceanics Niskin 6011 Mark II (tilt-type).

Time series

Time-series measurements were made in the 9603 and 9606 surveys. In March 1996, hourly time-series of CTD casts were made with the ship anchored at a place north of San Felipe [marked Z in Figure 3(g)] during neap and springs tides. Current meters were installed in March of 1996 at the positions marked by T (25 m of water) and Z (22 m) in Figure 3(g), both at 5 m above the bottom; the instrument at Z worked for only 3 days, and that at T (mainland side) sampled for 15 days. In June of 1996, current meter (at 1 m and 6 m above the bottom) observations and half-hourly CTD casts were made again North of San Felipe; the site is marked by D (water depth 22 m) in Figure 3(h). The time-series are 53 h long in spring tides and 58 h long in neap tides. Winds were measured at Punta Estrella (Figure 1), South of San Felipe, throughout 1995 and 1996. Table 1 summarizes the details of the current meter deployments.

Results

T/S diagrams

The T/S diagrams for the historical and new data sets [Figures 4(a),(b)] illustrate many of the features of the hydrography of the UGC. The apparent differences between the two data sets are due to differences in the surveyed areas: the historical data are only from the top 10 m, the new set does not include data from the Delta, but includes many profiles from Wagner Basin, and one from Delfin Basin, in order to put the UGC data in a regional perspective.

The seasonal cycle of the temperature is the most obvious feature: the surface layer temperature changes from about 15 °C in January to about 31 °C in August. The increase of temperature toward the shallower (saltier) water in summer and its crease in winter is also apparent. There is also a clear seasonal signal in salinity, with the maximum in August and minima from December to March. In addition to the seasonal signal of the density, the increase of density toward the shallowest (saltiest) water throughout the year is discernible. The water in the UGC is densest in December, January and February.

Hydrography and currents

In this subsection, the annual cycle of the hydrographic structure of the UGC is described, based on the best-sampled surveys of the new data set. Some limited but interesting current measurements are also presented. In the remainder of this paper, surface and

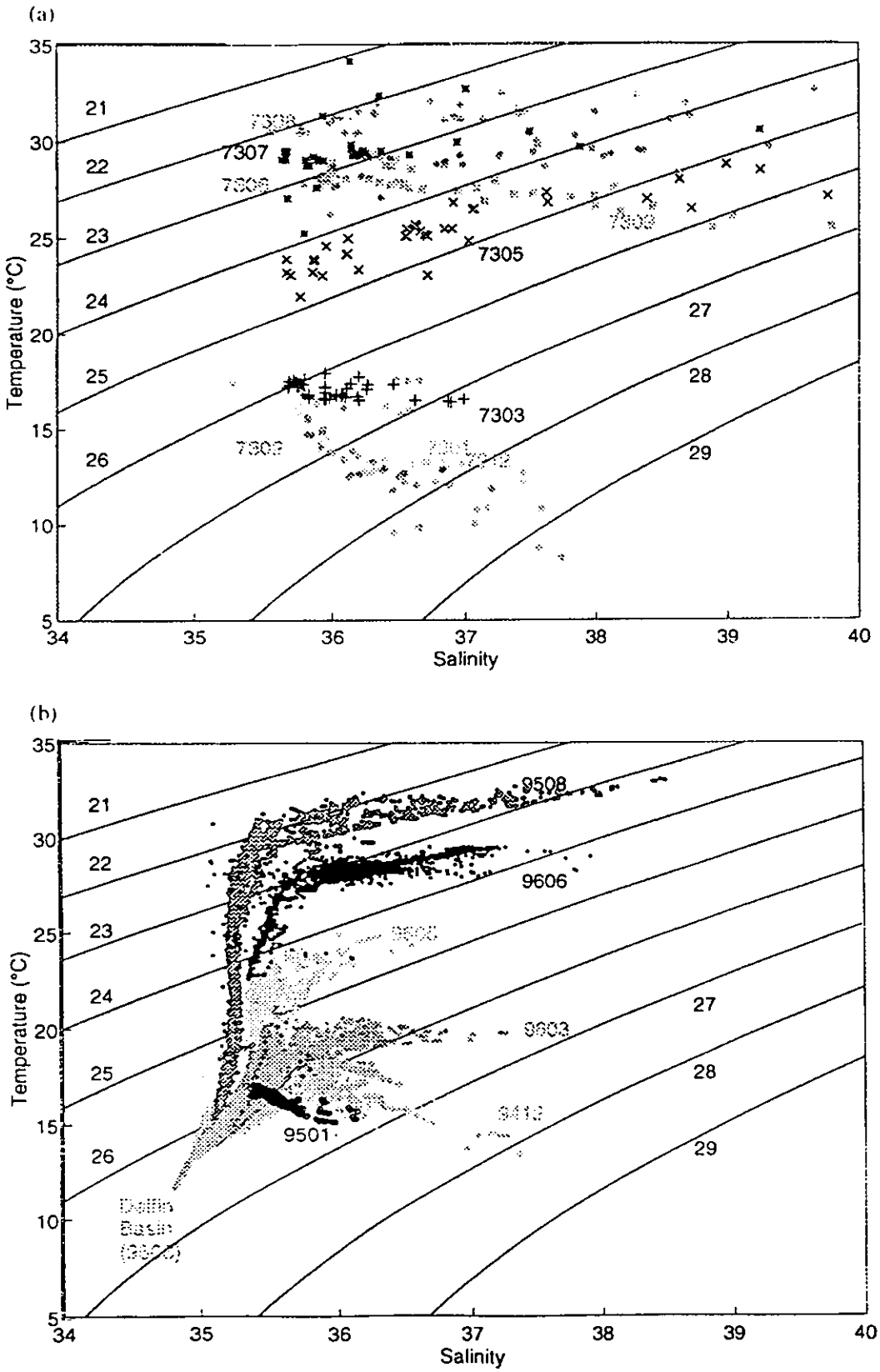

FIGURE 4. Temperature-Salinity diagrams for the Upper Gulf of California: (a) Historical data from December 1972 to September 1973 and (b) Data obtained between December 1973 and July 1976. The salinity of the historical data is in ppt and the new data is in ups; units are omitted in both cases.

bottom values of variables like temperature (T), salinity (S) and density (σ_t) will be denoted by subindices s and b, respectively. The difference of the surface minus the bottom values will be denoted by Δ (e.g. $\Delta T = T_s - T_b$).

Winter (7–17 December 1993). The distributions of temperature, salinity and σ_t [Figure 5(a),(b),(c)] show the pattern observed previously in the historical data, with the coldest ($\sim$15 °C), saltiest (36·7) and densest (27·2) water in the shallow, extended shelf on the peninsula side. The entire UGC was vertically homogeneous in the three variables [Figure 5(d),(e),(f)].

Spring (25 March to 9 April 1996). The distribution of surface salinity [Figure 6(a)] shows the increase toward the NW, where the maximum salinity (37·2) is found in a nucleus close to the Baja California (henceforth BC) coast. Adair Bay has salinity above 36. The distribution of ΔS [Figure 6(b)] shows vertical homogeneity almost throughout the UGC. The vertical contours of salinity (Figure 6) show that the high salinity nucleus is vertically homogeneous, except at the seaward edge, where $\Delta S \sim 0{\cdot}1$ [Figure 6(b)]. The tilt of the isohalines at the edge of the nucleus suggests that it extends as a near-bottom intrusion, with salinity decreasing outwards. At the eastern end of Line S4 there is an increase of salinity near the bottom, which may have originated further north, or locally in Adair Bay; this latter suggestion seems to be supported by the distributions of salinity at the eastern end of Lines S5 and S6.

The distribution of T, [Figure 7(a)] shows that the coastal water has begun to warm, with the distribution pattern in transition from winter to summer conditions. A streak of minimum temperature is found in the middle of the UGC. ΔT [Figure 7(b)] shows stable stratification in the UGC, of about 0·2 °C, while in Adair Bay the temperature profile is inverted with $\Delta T \sim -0{\cdot}1$ °C. The vertical cross-sections (Lines S1 to S4) show that the sites with high salinity water described above are also warm, both in the NW off BC and in Adair Bay. In the T and S fronts off BC, in lines S5 to S6, the isotherms tilt in opposition to the isohalines. The eastern end of Line S4 presents a temperature increase near the bottom, coinciding with the salinity increase. Extensive temperature stratification is present only in Lines S5 and S6. The boundary between the stratified and well-mixed areas is given approximately by the $\Delta T = 1$ °C isoline [Figure 7(b)], and coincides quite well with the frontal position predicted by Argote *et al.* (1995).

The distribution σ_t, [Figure 8(a)] shows that the densest water ($\sigma_t \sim > 26{\cdot}1$) is found at the NW corner of the UGC. $\Delta\sigma_t$ shows [Figure 8(b)] slight stratification ($\Delta\sigma_t \sim -0{\cdot}15$) in most of the UGC, with no inversions. The vertical cross-sections of density (Figure 8) follow very closely the salinity sections, the density maxima coinciding with the salinity maxima. The distribution of water with $\sigma_t > 26{\cdot}8$ (shaded in Figure 8) from Line S1 to Line S4 suggest that the densest water originated in the shallow BC side and moved as a near-bottom intrusion as far as Line S4. There is no water with $\sigma_t > 26$ elsewhere in the UGC.

The tides, currents and wind measurements made during this survey are shown in Figure 9. The tidal range in San Felipe varied from less than 1 m to almost 6 m [Figure 9(a)]. The currents measured at site T (black squares in Line S5, previous three figures) show [Figure 9(b)] tidal currents that reach 0·5 ms^{-1}, while the low-passed flow is only 0·04 ms^{-1} at its maximum [Figure 9(e)], which occurred during neap tides and was directed out of the UGC. The current meter data from the peninsula side (site Z) lasted too little to allow filtering [Figure 9(c)], but the fact that the flood is slower than the ebb suggests southward residual flow. There is no obvious correlation between the residual currents and the wind [Figure 9(f)]. the CTD time-series made at site Z (not shown) reveal well-mixed conditions both in spring and neap tides, with some near-surface temperature stratification in the afternoon.

Early summer (23 June to 1 July 1996. The shallowest sections, S1 and S2 were not sampled in this cruise, therefore the authors have only the three lines at the entrance to the UGC and S6, which passes through the edge of Wagner Basin.

The surface salinity [Figure 10(a)] increases from 35·6 in the entrance to over 36 in Adair Bay and up to 36·7 off the BC coast. In the BC zone there is a very pronounced salinity inversion (defined here as salinity increasing downward, which is the inverse of the normal vertical salinity variation in the Gulf of California) [Figure 10(b)], with the bottom salinity exceeding surface salinity by up to 0·5. The vertical sections of salinity S3 and S4 (Figure 10) show that the salinity inversion off BC is due to high salinity water from the coast extending over the bottom to the south and east, in what looks like a gravity current. In vertical sections S5 and S6, water with salinity between 36 and 37 hugs the BC coast, with the tilt of the isohalines decreasing to the south. There is also some high salinity water (>36) on the Eastern end of line S5 (Adair Bay), and also at the bottom on the eastern end of Line S4; the source of this bottom water is probably Adir Bay. The central part of sections S6, S5 and S4 have lower salinity (35·4),

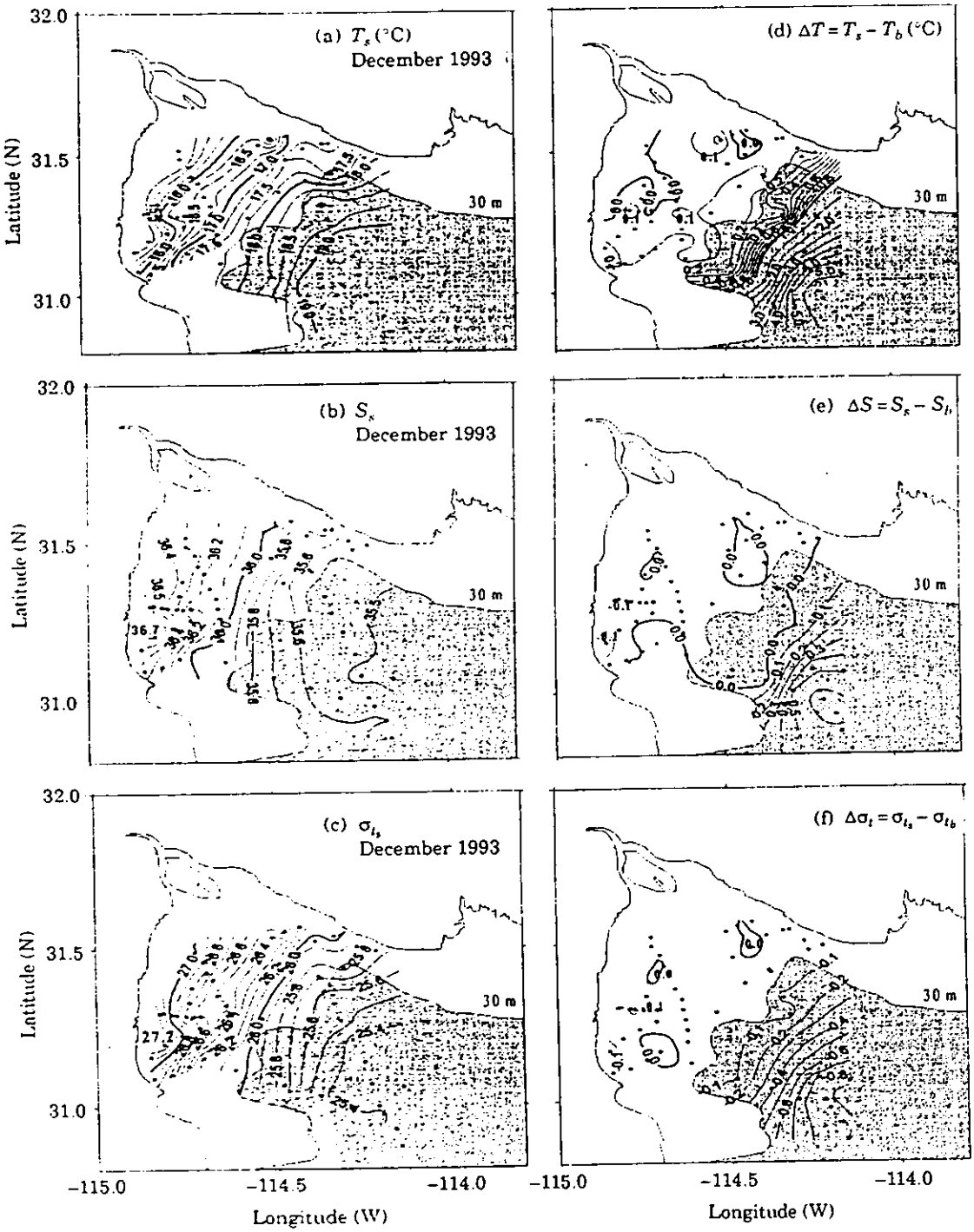

FIGURE 5. Hydrography of the UGC in December 1993: (a) surface temperature T_s; (b) surface salinity S_s; (c) surface σ_t; (d) surface to bottom temperature difference $T_s - T_b$; (e) surface to bottom salinity difference $S_s - S_b$; (f) surface to bottom density difference bottom density difference $\sigma_{t_s} - \sigma_{t_b}$. Areas deeper than 30 m is shaded.

indicating the influence of water from Wagner Basin.

The surface temperature [Figure 11(a)] shows the summer pattern, with the highest temperatures (29 °C) in the shallowest zone and the lowest (25 °C) at the entrance to the UGC. The ΔT distribution [Figure 11(b)] shows that the area off BC that had the salinity inversion also is inverted in temperature, with bottom water up to 0·5 °C warmer than that at the surface. Figure 11(b) also shows that the tidal mixing

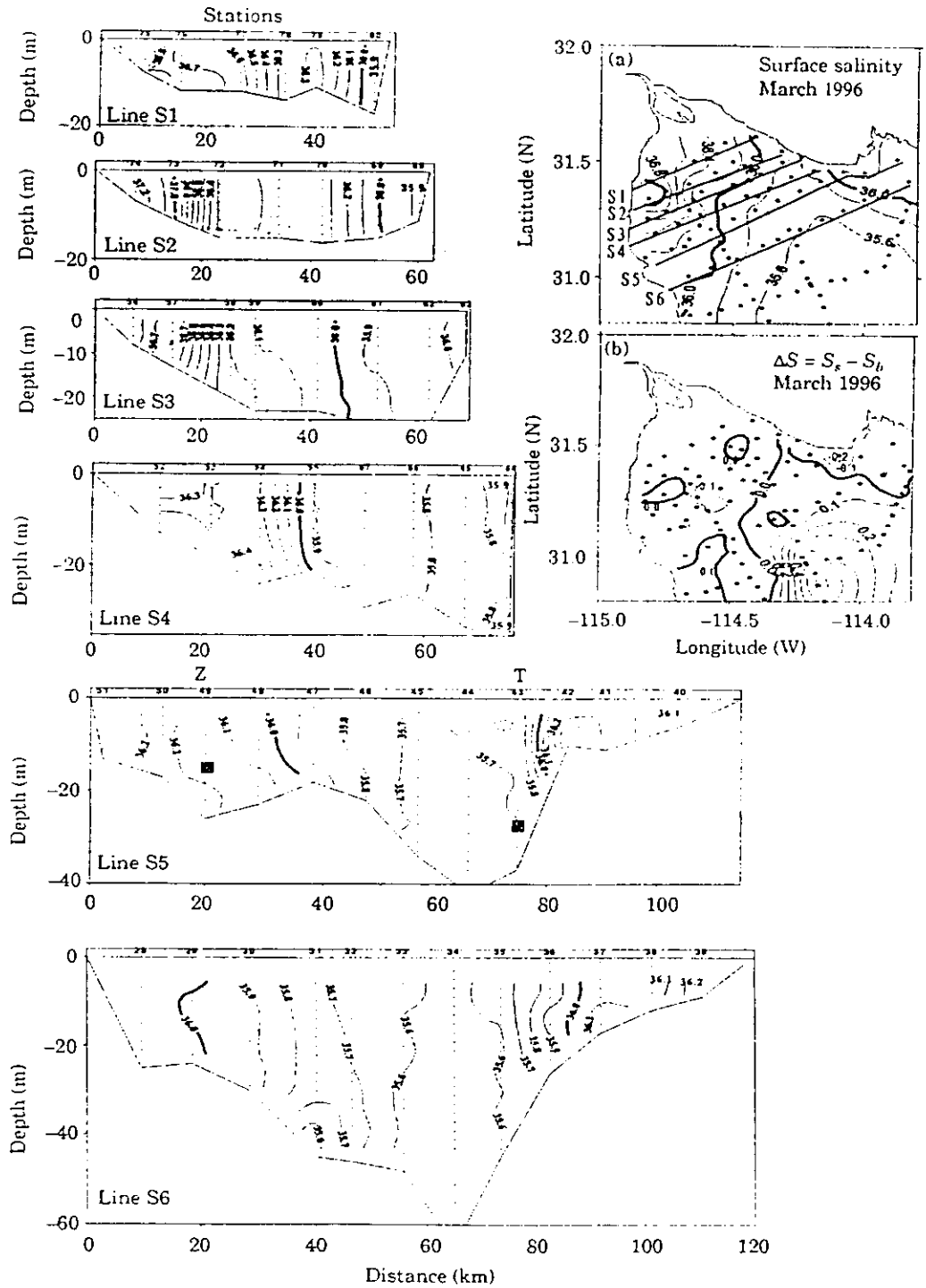

FIGURE 6. Distribution of salinity in the Upper Gulf of California in March 1996: (a) surface salinity; (b) surface to bottom salinity difference. Line S1 to Line S6: vertical cross-sections of salinity along the cross-gulf lines marked in (b). The black squares in Line S5 show the position of the current meters.

front (defined by $\Delta T = 1$ °C) is approximately at the same position as in spring. The vertical distributions of temperature (Lines S3 to S6, Figure 11) show that the isotherms off BC have the same tilt as the isohalines in the previous figure. The central part is influenced by cold, less salty water from Wagner Basin, while the BC coast and Adair Bay contain the warmest and saltiest water.

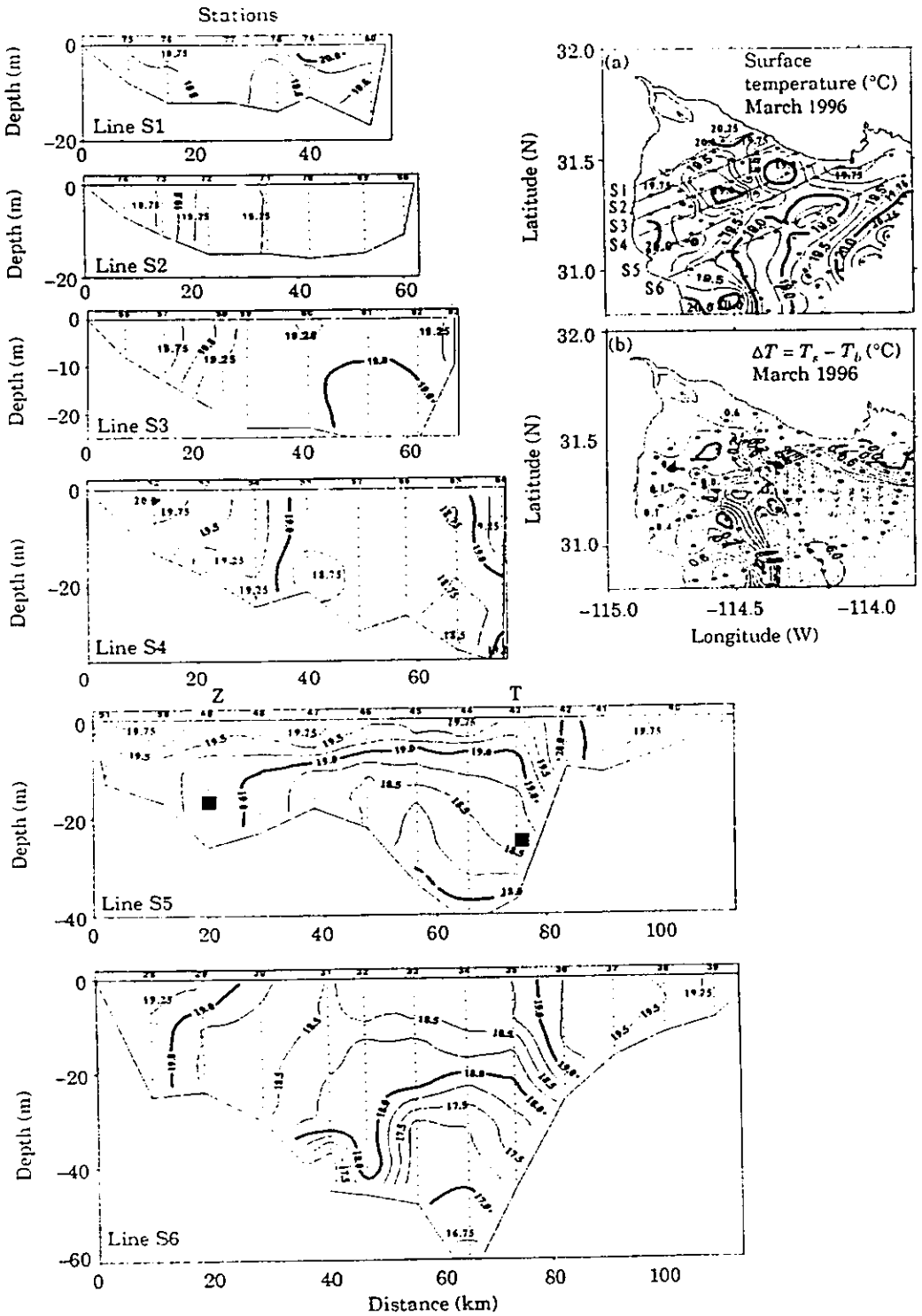

FIGURE 7. Distribution of temperature in the Upper Gulf of California in March 1996: (a) surface temperature; (b) surface to bottom temperature difference. Line S1 to Line S6: vertical cross-sections of temperature along the cross-gulf lines marked in (b). The black squares in Line S5 show the position of the current meters.

There is very little variation in surface σ_t [Figure 12(a)], with maxima in the coastal water off BC (23·4) and in the water from Wagner Basin at the centre of the entrance (23·6). All the area was stably stratified, with values of $\Delta\sigma_t$ up to $-0{\cdot}2$ in the UGC, and up to $-0{\cdot}6$ in the edge of Wagner Basin

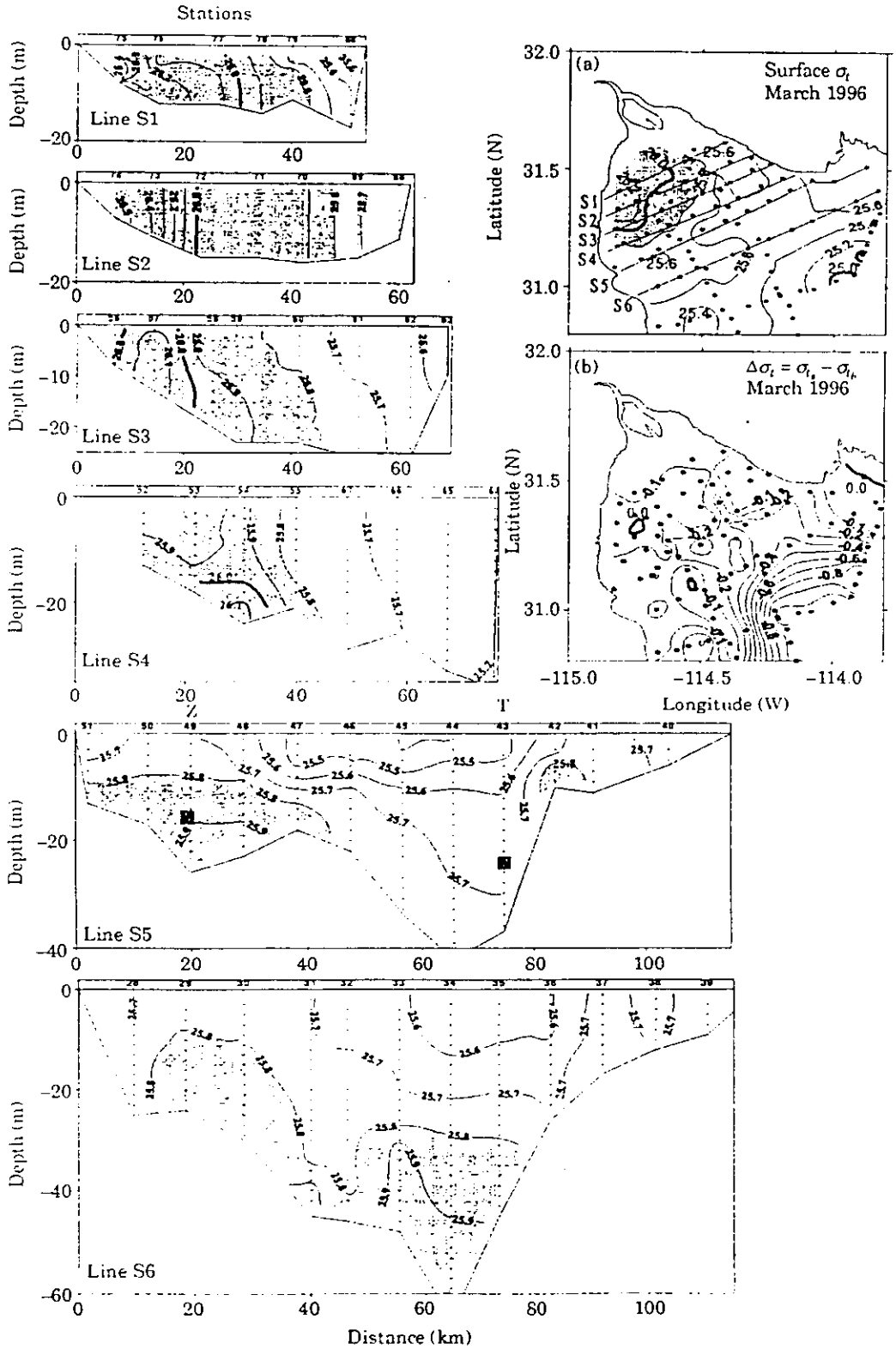

FIGURE 8. Distribution of σ_t in the Upper Gulf of California in March 1996: (a) surface σ_t; (b) surface to bottom σ_t difference. Line S1 to Line S6: vertical cross-sections of σ_t along the cross-gulf lines marked in (b). The black squares in Line S5 show the position of the current meters.

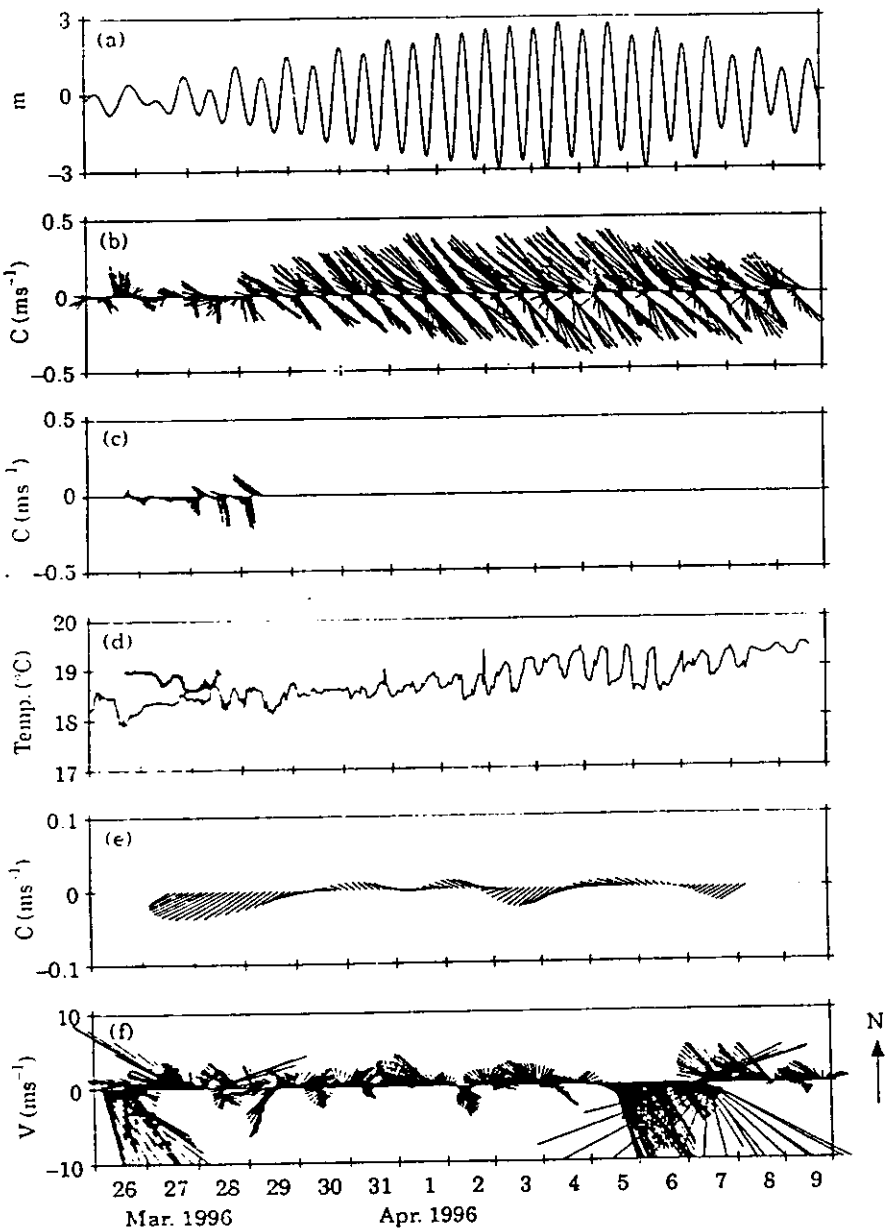

FIGURE 9. Time-series collected in the UGC between 26/03/96 and 09/04/96: (a) tidal height at San Felipe; (b) current velocity vectors 1 m above the bottom at site T; (c) current velocity vectors 1 m above the bottom at site Z; (d) water temperature measured by the current meters at site T (thin line) and site Z (thick line); (e) low-passed current velocity vectors at site T; (f) wind velocity vectors at Punta Estrella (Figure 1), drawn in oceanographic convention.

[Figure 12(b)]. The vertical distribution of density (Lines S3 to S6, Figure 12) reflects the salinity distribution in the West, and the temperature distribution in the deeper, central part. Although the isopycnals on the BC side of Lines S3 to S5 have the same inclination as the isohalines and the isotherms, the vertical gradients are not as strong; this is due to the opposing effects of both salinity and temperature increasing toward the bottom. In all the sections there is a zone of minimum density, sandwiched between the BC coastal high density (due to salt) and the offshore high density (due to temperature) water from Wagner Basin.

The neaps CTD time series [Figure 13(a)] was made on the edge of the patch of high salinity water (Site D Line S5, Figure 12), just before sampling the grid of stations. Initially the water was homogeneous ($T \approx 29{\cdot}4$ °C, $S \approx 36{\cdot}9$, $\sigma_t \approx 23{\cdot}4$), but soon became stratified with the appearance in the surface, of less dense, less warm and less salty water ($T \approx 28{\cdot}2$ °C,

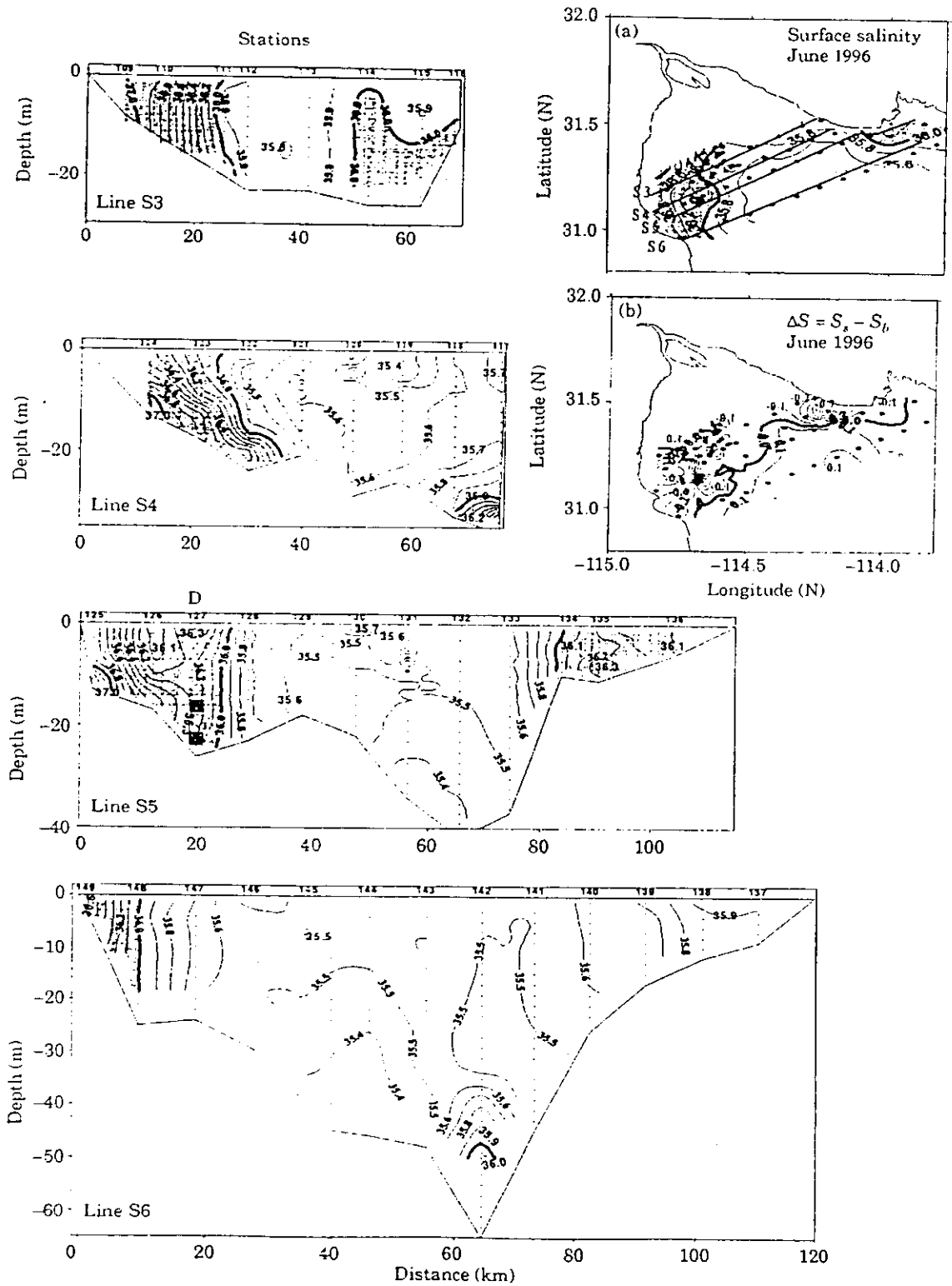

FIGURE 10. Distribution of salinity in the Upper Gulf of California in June 1996: (a) surface salinity; (b) surface to bottom salinity difference. Line S3 to Line S6: vertical cross-sections of salinity along the cross-gulf lines marked in (a). The black squares in Line S5 (Site D) show the position of the current meters.

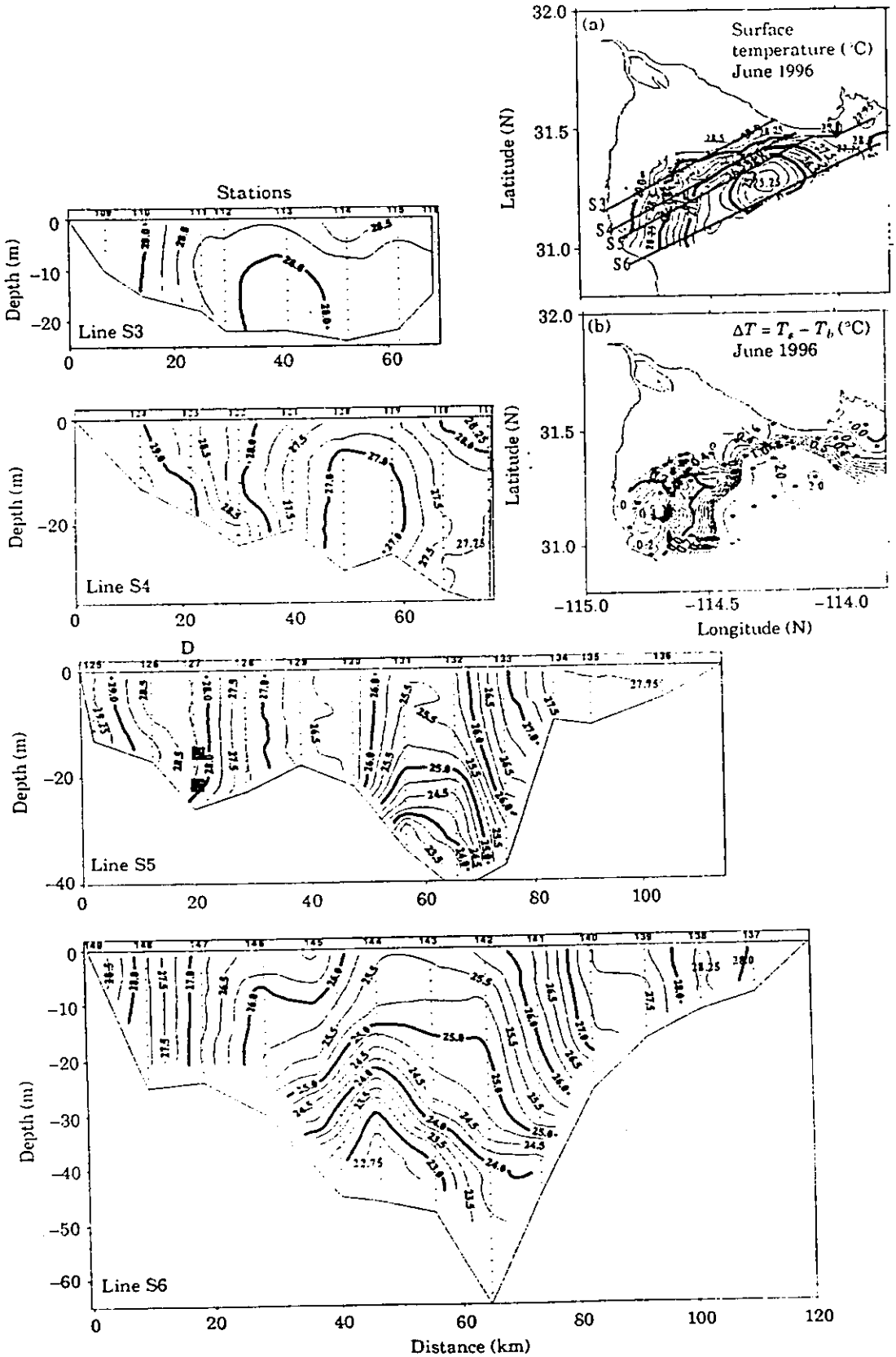

FIGURE 11. Distribution of temperature in the Upper Gulf of California in June 1996: (a) surface temperature; (b) surface to bottom temperature difference. Line S3 to Line S6: vertical cross-sections of temperature along the cross-gulf lines marked in (a). The black squares in Line S5 (Site D) show the position of the current meters.

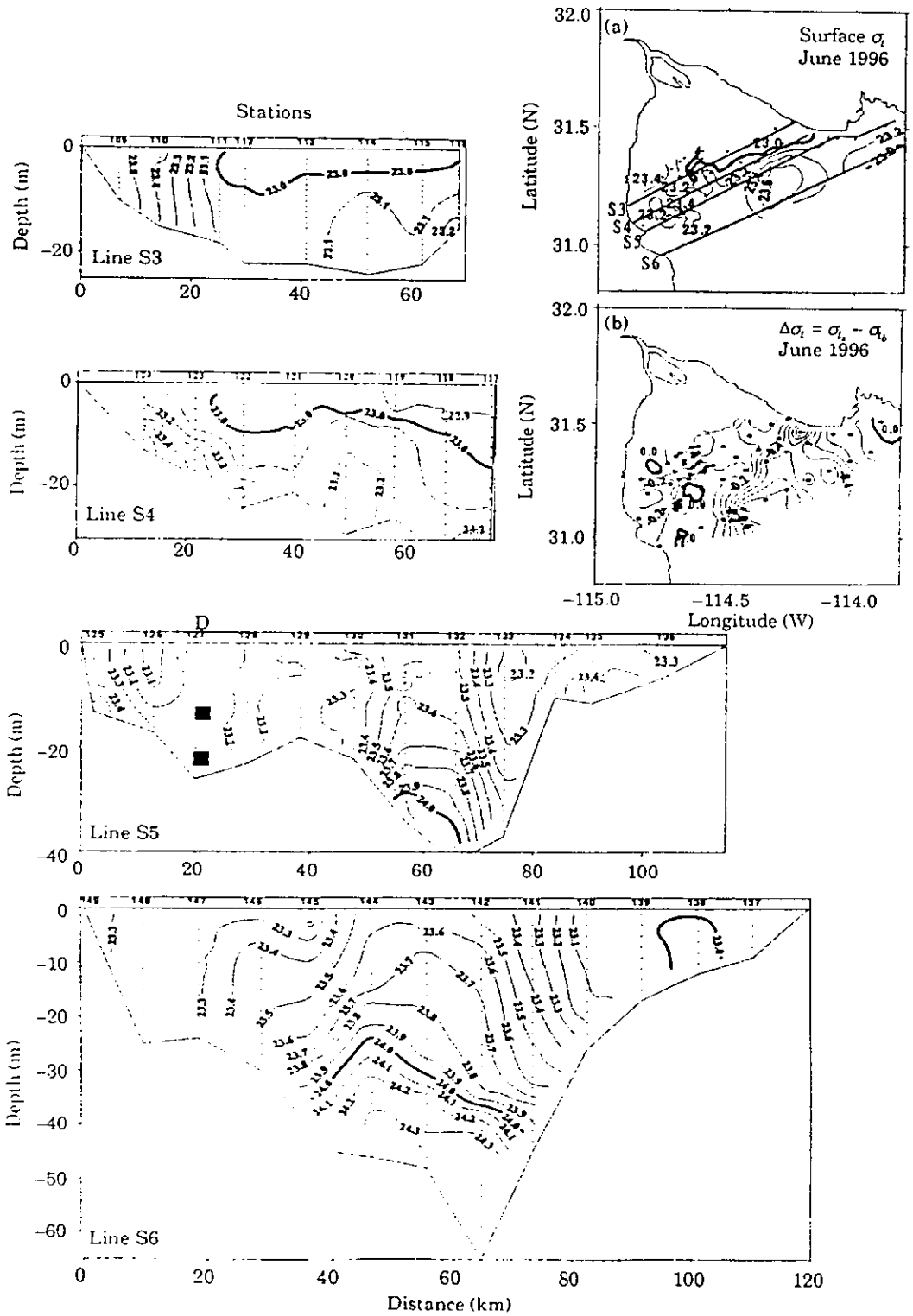

FIGURE 12. Distribution of σ_t in the Upper Gulf of California in June, 1996: (a) surface σ_t; (b) surface to bottom σ_t difference. Line S3 to Line S6: vertical cross-sections of σ_t along the cross-gulf lines marked in (b). The black squares in Line S5 (Site D) show the position of the current meters.

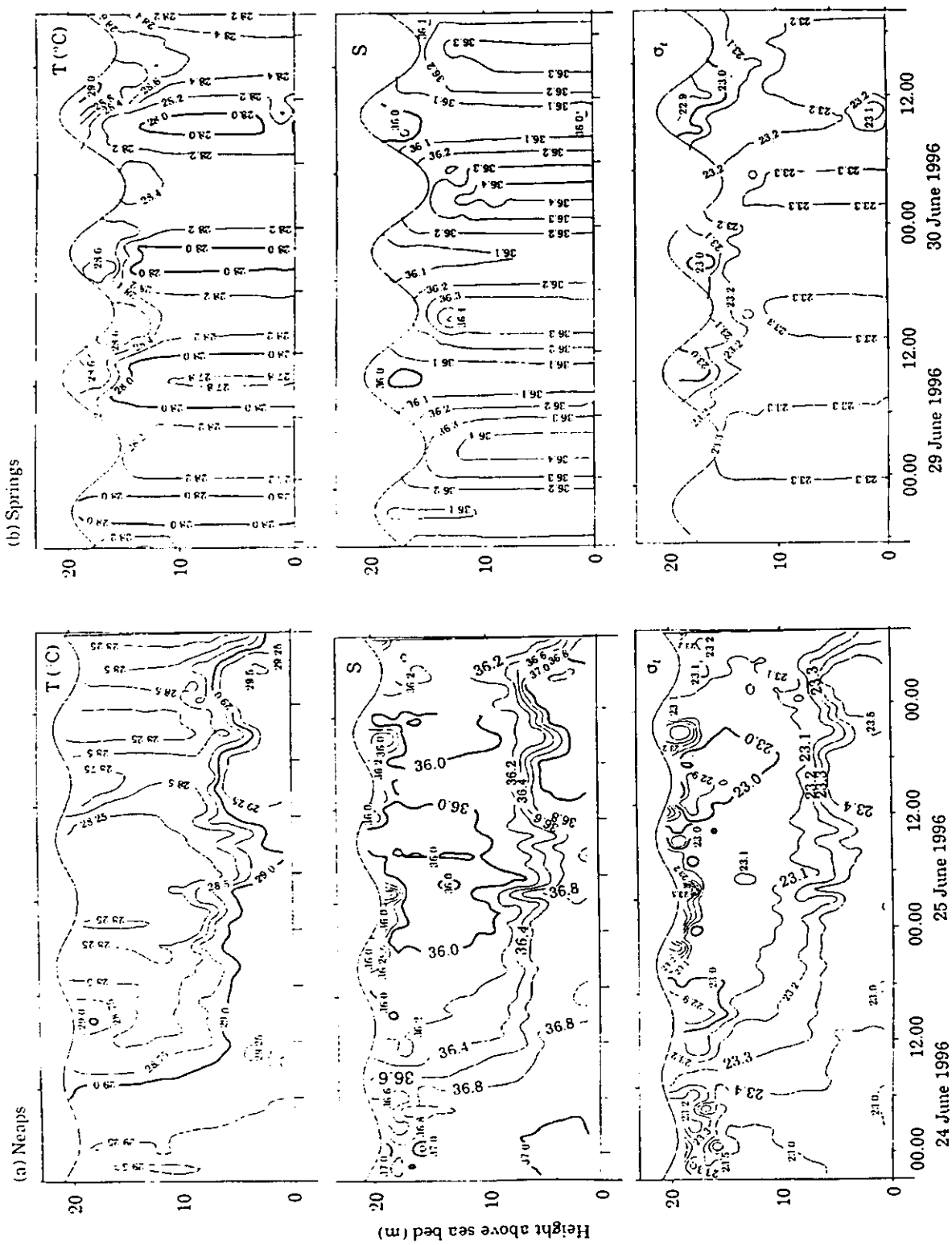

FIGURE 13. Time-series of CTD casts, made at site D, simultaneously with the current meter measurements of the next Figure (24–25 June 1996). On the left (a), the data for neaps tides shows very strong temperature and salinity inversions. On the right (b), the data for spring tides shows vertically mixed conditions.

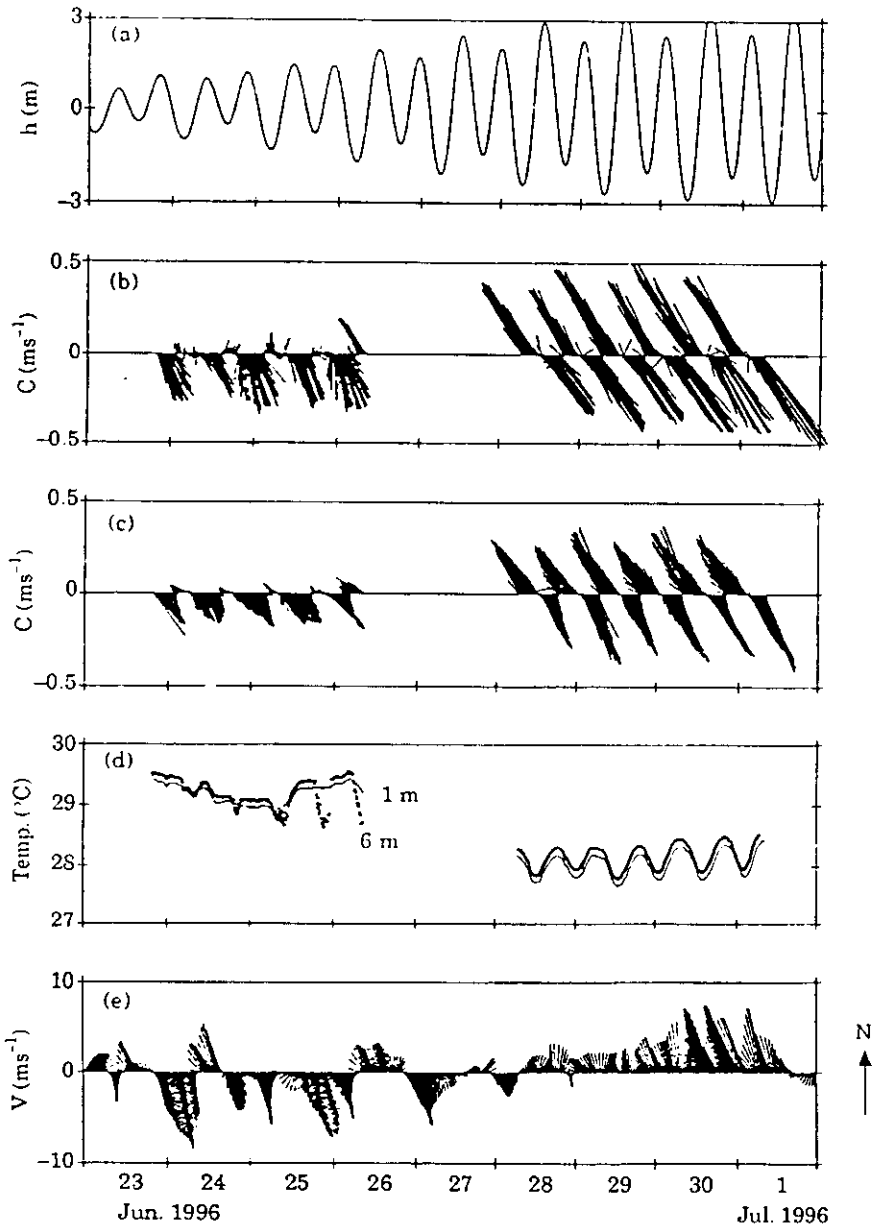

FIGURE 14. Time-series of sea level, currents and wind, made simultaneously with the current meter measurements of Figure 13 (24–25 June 1996): (a) sea level at San Felipe; (b) current vectors 6 m above the bottom at Site D; (c) current vectors 1 m above the bottom at Site D; (d) temperature at 1 and 6 m above the bottom at Site D; (e) wind vectors measured at Punta Estrella, drawn in oceanographic convention.

$S \approx 36{\cdot}0$, $\sigma_t \approx 23{\cdot}0$), while the properties of the initial homogeneous water are now found only in a 7 m-thick bottom layer. During the stratified period, which lasted for at least 40 h, salinity and temperature stratification were 0·4 and 0·6 °C, respectively, with $\Delta\sigma_t$ of about 0·4.

The current meter data collected at the same time as the neaps CTD time-series [Figure 14(a)] show that a residual current to the South completely arrests the flood tidal current [Figure 14(b) and (c)], both at 1 and 6 m above the bottom; the average speed over 2 tidal cycles is $\sim 0{\cdot}1$ ms^{-1}. More accurate estimates of the residual current can be obtained with Progressive Vector Diagrams, or by low-pass filtering the data shown in Figure 14(b) and 14(c), either filling the gaps with zeros or with predicted tidal currents; the results do not differ significantly at the centre of the sampled period. At 1 m above the bottom, the current is toward 141°, at 0·102 m s^{-1}; at 6 m above the bottom, the direction is 154° and the speed is

0·125 m s^{-1}. The 13° difference in direction suggests a bottom Ekman layer. The temperature records from the current meters [Figure 14(d)] show that at times the upper current meter was above the homogeneous bottom layer, as evidenced by the short-time pulses of temperature lower than at 1 m; this is congruent with the presence of internal waves in the pycnocline, which can be seen in the concurrent CTD data [Figure 13(a)].

The springs CTD time-series [Figure 13(b)] show almost well-mixed conditions, with $T \approx 28$ °C, $S \approx 36{\cdot}3$ and $\sigma_t \approx 23{\cdot}3$. There seems to be day-time near surface temperature stratification due to solar radiation. The currents measured during the spring tides [Figure 14(b) and (c)] reach up to 0·5 ms^{-1}, and are responsible for the almost well-mixed conditions. The average speed over five tidal cycles is very slow ($\sim$0·01 ms^{-1}). The mean shear between 1 and 6 m above the bottom is $\sim$0·02 s^{-1}. The current meters show that the temperature structure is now stable [Figure 14(d)], that it has fallen from $\sim$29 °C to $\sim$28 °C since the neaps observations, and that it has a tidal signal of 0 2 °C amplitude; all this is in agreement with the concurrent CTD date [Figure 13(b)].

The data suggest that during this summer survey a water-mass formation event was witnessed, and that the dense water formed in the region moved as a 7 m-thick bottom gravity current with speeds of about 0·1 ms^{-1}. This occurred during neap tides only, probably because the intense tidal stirring during spring tides inhibits the formation of a two-layer structure, and destroys that formed during neap tides. The neaps CTD time-series [Figure 13(a)] clearly shows the shape of the intruding head of lighter fluid in the upper layers; the bottom head of dense fluid does not show because the CTD data were taken on the warm, salty side of the (originally vertical) density front.

High summer (1–7 August 1995). As the T/S diagram [Figure 4(b)] shows, in this cruise was found the warmest, saltiest and least dense water. The surface salinity [Figure 15(a)] reaches 38·2 in the NW, while in the deeper central part, 35·4 salinity indicates the presence of water typical of Wagner Basin; in Adair Bay salinity rises again (36·4). The shape of the surface isohalines off the BC side suggest a tongue of the high salinity coastal water flowing South along the isobaths; in this area, the bottom salinity is higher than at the surface by about 0·2 [Figure 15(b)]. There is a central area in the UGC where S is vertically homogeneous [Figure 15(b)], but in most of it $\Delta S < 0$, while in Wagner Basin ΔS reaches 0·4. The vertical distribution of salinity (Lines S1 to S6, Figure 15) shows a zone of salinity maximum that starts in the shallowest NW area and extends slightly offshore all the way to section S6, where it is found in Station 5 as a subsurface nucleus of $S \approx 36$ at a depth of 20 m. From S4 to S6, the deeper area is occupied with water from Wagner Basin, with $S \approx 35{\cdot}4$. Salinity is high (>36) in Adair Bay, and again there is the suggestion, by the shape of the isohalines between Stations 25 and 26 (Line S5), that the S maximum at the bottom of Station 42 (Line S4) may have originated in Adair Bay.

The surface isotherms [Figure 16(a)] run across the axis of the UGC, except in the edge of Wagner Basin, where they follow the bathymetry. The warmest water (>32 °C) is in the NW side and in Adair Bay. Colder water lies at the bottom ($\Delta T \approx 0{\cdot}2$ °C), except in Adair Bay. [Figure 16(b)]. The vertical sections of temperature (Lines S1 to S6, Figure 16) clearly show the presence of Wagner Basin stratified water in the deeper part of the southernmost sections. The salinity maximum at the bottom of Station 5 (Line S6, Figure 16) does not have an associated temperature anomaly.

The surface density [Figure 17(a)] was about 22 in most of the UGC and in Adair Bay. The NW area again stands out, with a maximum of 23·2, and a suggestion of a southward-flowing tongue of dense water, clearly reflecting the salinity distribution [Figure 15(a)]. Stable conditions were found throughout the UGC [figure 17(b)], with $\Delta\sigma_t \approx 0{\cdot}1$. The vertical sections of density (Lines S1 to S6, Figure 17) follow those of salinity on the western side. The shadings in Figure 17 show the distribution of the water with $22{\cdot}3 \leq \sigma_t \leq 22{\cdot}6$ (light shading) and $22{\cdot}6 \leq \sigma_t \leq 23{\cdot}0$ (dark shading), illustrating that the density that corresponds to the salty water in the NW is found outside the UGC at a depth of $\sim$20 m. The core of high salinity, isothermal water found in Station 5 (Line S6, Figure 15) seems to have been generated close to the head, since its density (22·7) is present from Line S1 to Line S3 (Figure 17).

Discussion

Water-mass formation and gravity currents

Recent studies on water-mass formation in the Northern Gulf of California (Lavín *et al.*, 1995; López, 1997) suggest that the high-salinity water that is found in winter at the bottom of Wagner Basin comes from shallow areas like the UGC and Adair Bay, and that upon leaving the formation area, the newly formed water moves as a gravity current along

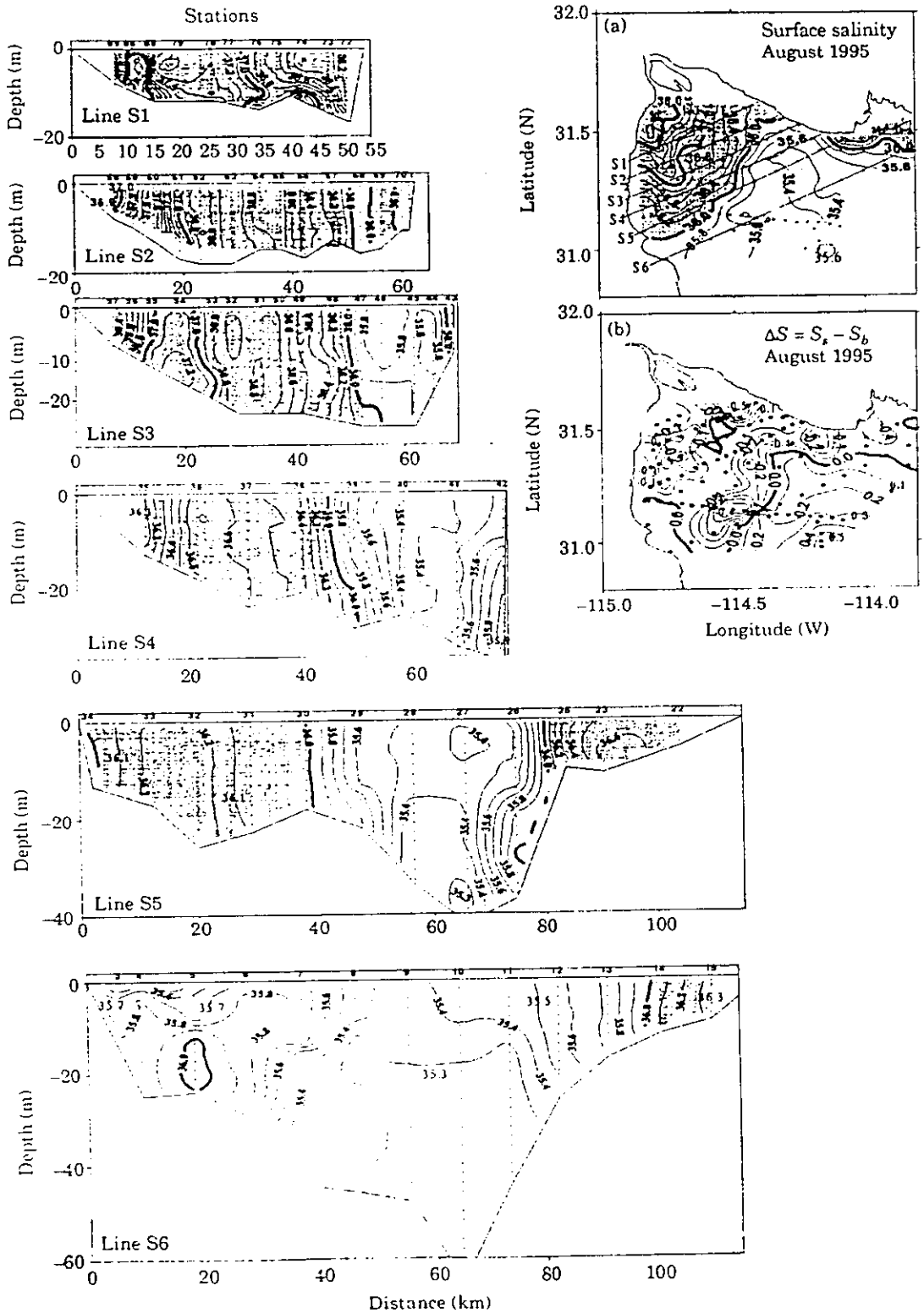

FIGURE 15. Distribution of salinity in the Upper Gulf of California in August 1995: (a) surface salinity; (b) surface to bottom salinity difference. Line S1 to Line S6: vertical cross-sections of salinity along the cross-gulf lines marked in (a).

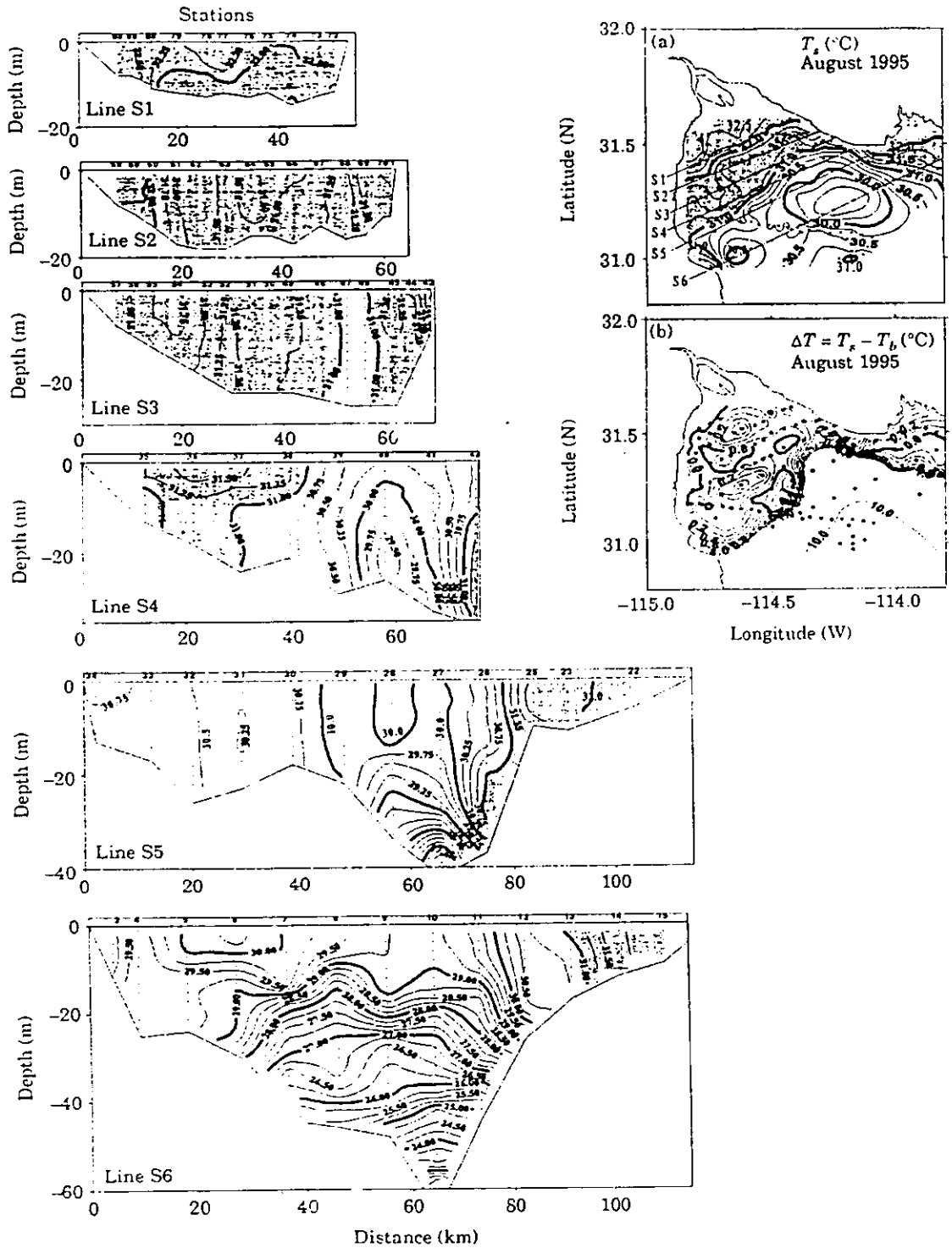

FIGURE 16. Distribution of temperature in the Upper Gulf of California in August 1995: (a) surface temperature; (b) surface to bottom temperature difference. Line S1 to Line S6: vertical cross-sections of temperature along the cross-gulf lines marked in (a).

the isobaths, with the shallow water to the right of the motion. However, no observational or numerical studies of water mass formation have hitherto been performed on the UGC proper.

In the T/S diagrams of the UGC (Figure 4), for all months there are isopycnals that cross the T/S diagrams at two places. The isopycnal that touches the tip of the high-salinity end of the diagram crosses it again

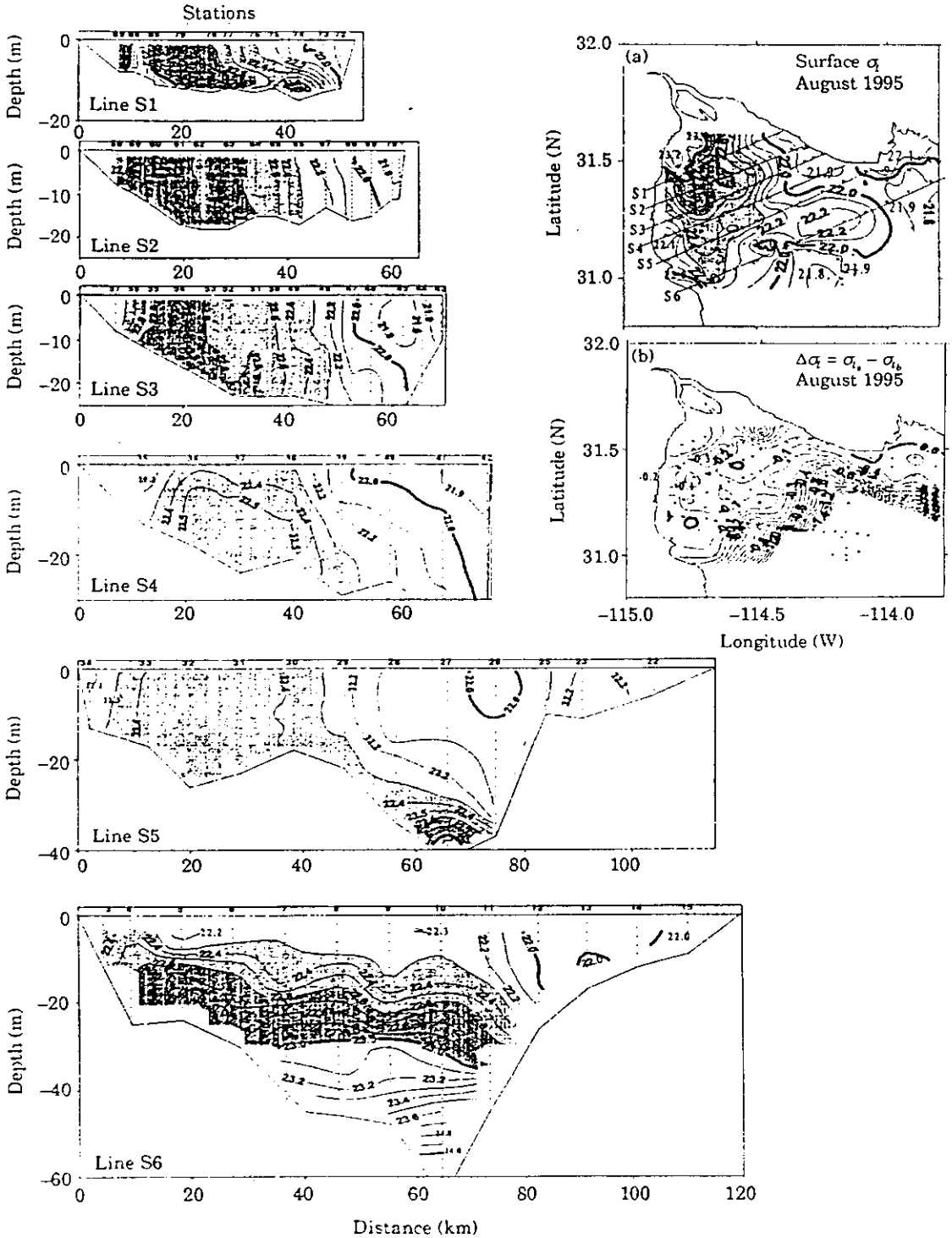

FIGURE 17. Distribution of σ_t in the Upper Gulf of California in August 1995: (a) surface σ_t; (b) surface to bottom σ_t difference. Line S1 to Line S6: vertical cross-sections of σ_t along the cross-gulf lines marked in (b).

at a place, which is below the surface, where the salty water from the UGC would find its equilibrium position (in the absence of entrainment) after going through the process of convection. The phenomenon has been documented in the Northern Gulf for winter (Alvarez-Borrego & Schwartzlose, 1979; Lavín *et al.*, 1995), but the possibility of its occurrence in summer, suggested by Figure 4, had not been considered before.

Water-mass formation is a widespread phenomenon in high latitudes, and it also occurs in a few

TABLE 2. Characteristics of the Upper Gulf of California and the South Australian Gulfs

	Upper Gulf of California[a]	Spencer Gulf[b]	Gulf St Vincent[c]
Area (km^2)	4500	19 500	7000
Mean depth (m)	20	22	25
Latitude	31°N	32°S	33°S
E ($m\ year^{-1}$)	1·1	1·0	1·7
Tidal currents	M_2=0·28	M_2=0·09	M_2=0·25
major semiaxis	S_2=0·21	S_2=0·10	S_2=0·27
(ms^{-1})	K_1=0·03	K_1=0·22	K_1=0·05
	O_1=0·02	O_1=0·11	O_1=0·04
Wind (ms^{-1})	Winter 8–12	Winter 3–10	Winter 3–10
	Summer 2–6	Summer 3–10	Summer 3–9
Head	Summer 33	Summer 24	Summer 24
T (°C)	Winter 8	Winter 12	Winter 13
Head	Summer 40	Summer 48	Summer 42
S	Winter 36	Winter 43	Winter 39
Head	Summer 29·2	Summer 33·0	Summer 28·8
σ_t	Winter 23·5	Winter 33·5	Winter 29·7
Mouth S	35·4	35·9	36·5
$\partial\rho/\partial y$ (kgm^{-4})	$2{-}6 \times 10^{-5}$	5×10^{-5}	$4\ 10^{-5}$

[a]Data from: Alvarez Borrego *et al.* (1973), and this publication.
[b]Data from: Nunes-Vaz *et al.* (1990) and references therein. Also pers. comm. R. Nunes-Vaz (1998).
[c]Data from: Provis and Lennon (1983), De Silva Samarasinghe and Lennon (1987), De Silva Samarasinghe (1989).

semi-enclosed seas, like the Mediterranean, the Red Sea and the Adriatic, where evaporation produces very high salinities. However, the conditions of the UGC are most similar to those of the South Australian gulfs (see Table 2), where the physics of warm-water inverse estuaries has been extensively investigated (see: Nunes Vaz *et al.*, 1990, and references therein). In these inverse estuaries, gravity currents generated by the water-mass formation process are a very important component of the regional oceanography.

Gravity currents in inverse estuaries are due to the pressure gradient induced by the increase of density toward the head: the dense, salty water slips under (and is replaced at the surface by) the lighter offshore water. Initially, the gravity current is in the direction of the pressure gradient, being affected only by friction with the bottom and the surrounding water: the water flows downslope across the isobaths, seeking the depth where the surrounding water has the same density. Within a time scale of $2\Pi/f$ ($\sim$1 day in the UGC, equivalent to a length scale of $\sim$10 km), the gravity current should be deviated to the right (in the Northern Hemisphere) by Coriolis force. When geostrophic balance is achieved, the flow is along the isobaths with the shallow water to the right of the motion. Friction induces cross-isobath motion, and the water keeps sinking until its density matches that of the surroundings (see Griffiths, 1986; or Bowers, 1989), and references therein).

Summer The current meter and CTD time-series collected during neap tides in June 1996 (Figures 14 and 13) show the evolution of a density current, with an estimated speed of $\sim$0·1 ms^{-1}. This speed is much stronger than those estimated with numerical models for wind forcing (0·01–0·03 ms^{-1}; Argote *et al.*, 1998), and for tidal rectification ($\sim$0·01 ms^{-1}, Marinone, 1997; Argote *et al.*, 1998).

The relationship between the bottom density distribution, the gravity current and the bathymetry is shown in Figure 18. The residual flow is approximately normal to the bottom isopycnals, and its angle with the local bathymetry is about 7° at 6 m and 21° at 1 m above the bottom.

The steady-state equations for a gravity current in a *uniformly sloping bottom* are (Bowers & Lennon, 1987):

$$\text{Along-flow balance:} \quad g'\alpha \sin\theta = ku^2/h \qquad (1)$$

$$\text{Across-flow balance:} \quad g'\alpha \cos\theta = fu, \qquad (2)$$

where u is the speed of the gravity current, f is the Coriolis parameter ($7{\cdot}29\ 10^{-5}\ s^{-1}$ at 31 °N), g' is the reduced gravity, h is the thickness of the layer, α is the slope of the interface (which is also the bottom slope),

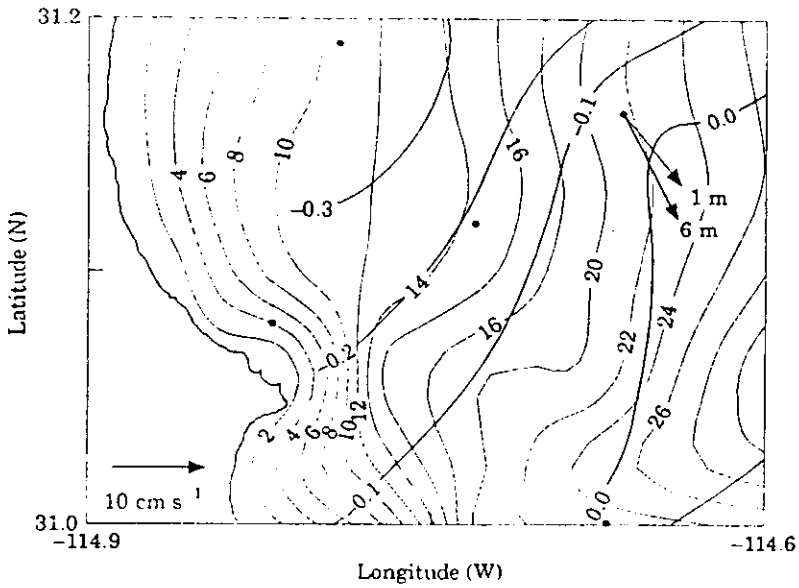

FIGURE 18. Relationship between gravity current, density structure and bathymetry in June 1996. Arrows are the residual currents at Site D during neap tides. The thin contours are the bathymetry in metres, and the thick contours are bottom σ_t. The small dots are the CTD stations.

Θ is the angle between the current and the isobaths and k is a friction coefficient ($\sim 0{\cdot}006$; according to Bowers & Lennon, 1987). The two equations allow the calculation of twos of the three parameters u, k or Θ, given the other one.

Although the CTD survey was made (immediately) after the neaps RCM measurements, let's assume that the gravity current was generated by a density distribution not very different to that shown in Figure 12. From the density cross-section at Line S4, Figure 12: $g' = 4 \times 10^{-3} \mathrm{ms}^{-2}$, h 7 m [see also Figure 13(a)], $a = 20$ m/20 km $= 10^{-3}$. Taking $\Theta \approx 15°$ (the calculation is not very sensitive to Θ), the geostrophic balance (2) gives $u = 0{\cdot}053\ \mathrm{m\,s}^{-1}$, which is in reasonable agreement with the observations. Since k is the most poorly known parameter, Equation 1 and the measured values of u and Θ can be used to calculate that k 0·0026.

These orders of magnitude are encouraging, but we don't have enough information to establish how close to geostrophic balance the situation was during sampling. This is determined from Θ; for instance, before geostrophic balance is reached, the flow is across the isobaths ($\Theta = \Pi/2$), and the along-current equation becomes $u = (g'h\alpha/k)^{1/2}$. With $k \approx 0{\cdot}003$, $u \approx 0{\cdot}10\ \mathrm{ms}^{-1}$, which is very close to the observed residual currents. Unfortunately, as Line S5 Figure 12 shows, the current meters were in a bathymetric depression, which may have affected the observed direction of the gravity current. This doesn't allow a good comparison with the simple theory presented above. It is clear that a better data set is needed.

By the time CTD and current meter time-series were resumed during spring tides (Figures 13 and 14), the T and S inverted conditions had disappeared and there was no strong residual flow (the average over 5 tidal cycles is only $0{\cdot}01\ \mathrm{ms}^{-1}$). It is proposed that the hydrographic conditions and the gravity current observed during neap tides disappear during spring tides due to the increased vertical mixing. The formation of gravity currents in inverse estuaries and their inhibition by vertical mixing have been studied in the laboratory (Linden & Simpson, 1986, 1988; Simpson & Linden, 1989) and their presence in nature has been documented in the South Australian Gulfs (de Silva Samarasinghe & Lennon, 1987; Nunes Vaz & Lennon, 1987; de Silva Samarasinghe, 1989; Nunez Vaz *et al.*, 1989, 1990). In these gulfs, neap tidal currents are very small and $\Delta\sigma_t$ reaches $-1{\cdot}0$; if the neap tides and calm coincide, the dense water in the interior of the gulf flows out, reaching a geostrophic balance with current speed of $\sim 0{\cdot}1\ \mathrm{ms}^{-1}$. In the Australian gulfs this occurs in both winter and summer (Nunes Vaz & Lennon, 1987), but the effects are more clearly seen and the gravity current reaches much farther and deeper during autumn and winter (Lennon *et al.*, 1987; Nunes Vaz *et al.*, 1990).

In summary, the summer observations show that vertical convection occurs during summer in the shallowest part of the UGC, that gravity currents are generated, and that they may be fortnightly modulated. None of these phenomena had been reported before for summer–autumn in the UGC.

ME: ecss PAGE: 24 SESS: 11 OUTPUT: Thu Sep 17 11:03:53 1998
journals/academic/56new/80387

TABLE 3. Properties of the surface and bottom water in Wagner Basin, for selected winter–spring cruises

Cruise→	Dec. 1993	Dec. 1994	Jan. 1990	Jan. 1995	Mar. 1973	Mar. 1988	Mar. 1996
S_s	35·60	35·47	35·45	35·41	35·35	35·31	35·50
S_b	34·97	**36·14**	35·15	**35·61**	**35·50**	**35·50**	35·00
T_s (°C)	19·30	18·18	16·50	16·74	16·50	15·00	19·50
T_b (°C)	13·47	17·20	14·00	16·16	15·00	14·67	13·50
σ_{ts}	25·41	25·59	25·97	25·89	25·90	25·90	25·20
σ_{tb}26·28	26·34	26·30	26·18	26·45	26·41	26·30	
$\sigma_{ts}-\sigma_{tb}$	− 0·87	− 0·78	− 0·33	− 0·29	− 0·45	− 0·51	1·10

Surface values with *s* subindex; Bottom (200 m) values with *b* subindex. Bottom salinities in **bold** type indicate the cases when the salinity at the bottom of Wagner Basin was higher than at the surface.

Winter-Spring The two previously reported observations of winter high-salinity water in the bottom of Wagner Basin (Alvarez-Borrego & Schwartzlose, 1979; Lavín *et al.*, 1995), presumably originating in the UGC, both occurred during the month of March, which may suggest that March is the month in which the most extensive convection occurs in the UGC. But there have been March data showing no extensive water mass formation; e.g. 1939 and 1985 (Sverdrug, 1941; Bray, 1988). In addition, the T/S diagrams of the UGC show (Figure 5) that by March the temperature of the UGC is several degrees above the winter minimum, and its density has decreased correspondingly. Also, by March the surface heat flux in the UGC has become positive (Reyes & Lavín, 1997). The apparent rapid thermal response of the UGC may be due to the shallowness of the area, and also to the flushing generated by the gravity currents.

The surface and bottom values of salinity, temperature and σ_t in Wagner Basin as measured in cruises between December and March are shown in Table 3. The Wagner Basin bottom water of coastal origin had temperature just under 15 °C in March 1988, and about 16·5 °C in March 1973; in both occasions salinity was about 35·5, and σ_t exceeded 26·3. In March 1996, no high-salinity bottom water was found in Wagner Basin: although high salinity was present in the UGC (>36, Figure 6), the water was not dense enough to sink to the bottom of Wagner Basin because its temperature was high (T ~19·5 °C, Figure 7). However, high salinity bottom water was found in Wagner Basin in December 1994 and January 1995 (Table 3): this is the first reported occurrence of the phenomenon in months different from March.

As Table 3 shows, there is much variability in the properties (T, S, σ_t) of the high-salinity water that reaches the bottom of Wagner Basin. A possible explanation for this variability is as follows: water-mass formation takes place throughout the year, with (sporadic) gravity currents taking the high-salinity water out of the UGC at a greater and greater depth as the seasons progress from summer to winter and the density of the formed water increases as shown, e.g. in the T/S diagrams (Figure 5). Evidence for this is the frequent presence (in CTD casts taken in Wagner and Delfín Basins) of mid-depth layers of high salinity, as reported by Bray (1988), by Lavín *et al.* (1995) and by López (1997)).

However, because of the shallowness of the UGC, the density of the water responds strongly to variability in the surface heat losses; this variability is controlled by the meteorology, which in turn has wide interannual variations (Reyes & Lavín, 1997). Therefore the month in which water is formed (and its T, S and σ_t) with high enough density to reach the bottom of Wagner Basin probably depends on the meteorology. The evidence presented here suggests that March may not be the month in which the phenomenon occurs most years. The surface fluxes of heat and moisture and the seasonal cycles of temperature and salinity (Figure 5) favour the months of December to February, which are the months in which density is maximum, but the year to year variations can be very wide.

Although no data are available from October and November, the T/S diagrams (Figure 4) indicate that these are the months when the annual salinity maximum (reached in August) is flushed from the top of the UGC. It is possible that the most extensive gravity current flushing takes place at this time, when the extremely salty water is cooled. But since it is still warm, its density is not high enough to reach the bottom of Wagner Basin, and remains in mid-depth layers.

Stratification

In the hydrographic observations in grids of stations and in the CTD time-series, slight stratification was present, with $\Delta\sigma_t \approx -0{\cdot}2$, except in winter [Figure 5(f)]. The presence of this slight, probably sporadic, stratification seems to be in disagreement with the prediction by Argote *et al.* (1995) that the UGC should be well-mixed throughout the year; it is a question of time-scales and non- parameterized phenomena. For instance, the largest observed stratification $\Delta\sigma_t \approx -0{\cdot}4$, occurred during the neaps CTD time-series of June 1996 [Figure 12(a)], but as explained before, it was due to the subsurface gravity current of high salinity.

The analysis of Argote *et al.* (1995) is an energy balance in a time-scale of months, of the mixing tendency due to the M_2 tidal currents and the stratifying tendency due to surface heating. The apparent widespread presence of slight stratification [Figures 8(b), 12(b) and 17(b)] in the UGC may be due to the fact that most of the CTD stations were made during neap tides. Apart from the neap-tides stratification associated with the gravity currents, diurnal thermoclines can be formed close to the surface at the times of maximum insolation (Figure 13).

Through direct straining of the horizontal density field, vertical shear in the tidal currents can introduce periodic stratification, depending on the horizontal density gradient and the vertical gradient and intensity of the tidal currents (Simpson *et al.*, 1990; Nunes Vaz & Simpson, 1994). From the current meter observations made at 1 and 6 m above the bottom in the spring tides between June 28 and July 1, 1996 (Figure 14), the mean vertical shear is calculated at $0{\cdot}02\ s^{-1}$. If it is assumed that the vertical profile is given by (Bowden & Fairbairn, 1952) $u(z) = 1{\cdot}15-0{\cdot}425(zh^{-1})^2)$, the amplitude of the difference between 1 m above the bottom and the surface is $0{\cdot}2\ ms^{-1}$. This is equivalent to a surface tidal excursion of 1·5 km, relative to 1 m above the bottom. The horizontal gradients of σ_t in the zone [Figure 12(a)] are of order 0·2 10 km; therefore, no significant stratification can be introduced by this mechanism.

Geographic distribution and circulation

The most obvious feature of the horizontal distribution of the hydrographic variables T, S and σ_t is the tendency for the extreme values to occur in the NW of the UGC: all the surface distributions show isolines with a N or NNE orientation, in both data sets. This was noted by Alvarez-Borrego and Galindo-Bect (1974), who proposed that it was an indirect evidence of a cyclonic residual circulation in the UGC. Although this is a reasonable proposition, inferring residual circulation from horizontal distributions of properties can lead to erroneous conclusions under certain circumstances (Hunter, 1975). In the case of the UGC, the inference certainly deserves close scrutiny, since the isolines also seem to reflect the bathymetry. In the similar case of the South Australian Gulfs, the distribution of salinity departs markedly from the bathymetry pattern (Nunes Vaz & Lennon, 1986); in this case the geographic distribution of variables has been proved by direct current measurements to be caused by the residual circulation (Nunes Vaz *et al.*, 1990).

The western, peninsular side of the UGC is much shallower, the bottom slope is much gentler, and it is farther from Wagner Basin than the SE part. This alone can explain the distributions, without recourse to a residual circulation; given a rate of evaporation E and of surface heat flux Q, the change of salinity (δS) and temperature (δT) in a time interval δt is larger the shallower the depth of the water column (h), since $\delta T = Q\delta t/(\rho C_p h)$, and $\delta S = SE\delta t h^{-1}$ (where ρ is the density and C_p is the specific heat of water). Therefore the isotherms and isohalines will follow the isobaths, with extreme values in the shallowest water. The eastern side of the entrance not only is deeper and the bottom slope very pronounced off the mainland coast, but Wagner Basin is a large reservoir of relatively low salinity (<35·4), which can be diffused laterally and vertically. The distribution of the low salinity water follows the depth contours in this area, and the distributions of salinity across the entrance to the UGC clearly show the presence of water from Wagner Basin [Figures 5(b), 6, 10 and 15]. However, the isolines are not exactly parallel to the isobaths, and the small difference could be due to residual circulation. In Figures 10 and 15 the trend of the isohalines seem to reflect the gravity currents.

Conclusions

Like other negative estuaries, in the UGC the salinity increase toward the head causes the density to do likewise; this occurs throughout the year, despite the seasonally reversing temperature gradient. The pressure gradient thus formed leads to gravity currents: in the case observed, the dense, salty water slipped under the lighter offshore water as a 7 m thick bottom layer at a speed of $\sim 0{\cdot}1\ ms^{-1}$. The gravity currents appear to be modulated by the available TKE, mainly form the tidal currents, but wind stirring is likely to be of importance. These currents, although

sporadic, are significantly faster than the wind-induced and tide-induced residuals, and they occur precisely when the tides and the winds are at their weakest.

Evidence of summer water mass formation in the UGC is presented here for the first time. While in winter water with the same density (σ_t>26) as that formed in the UGC is found south of Wagner Basin at depths exceeding 200 m (Lavín *et al.*, 1995), in summer water with $\sigma_t \sim 23{\cdot}4$ is found near the entrance to the UGC at a depth of only 20–30 m (Figures 15 and 17).

The results presented here confirm that the UGC is the source of the high-salinity water that is frequently found during winter at the bottom of Wagner Basin and further south. Adair Bay was also seen to produce high-salinity bottom water, and some salty bottom water may also be formed in the shallow shelf (<30 m deep) off mainland México.

In the vertical dimension, slight stratification $\Delta\sigma_t \approx O(-0{\cdot}2)$ was encountered in most of the surveys, which were made in neap tides. It is proposed that this stratification is sporadic, due to vertical convection of coastal dense water, and to solar radiation. Shearing stress of the tidal currents seems to be unimportant in generating periodic stratification.

Although limited, the data provide tantalising evidence of mixing-modulated gravity currents, but longer time-series and more detailed studies of the structure and properties of these currents are needed.

Acknowledgements

This work was funded by CICESE, and by CONACYT through Contracts No. 25555-T9712 and 3007P-T9606, and a postgraduate scholarship for Victor M. Godínez. This paper was finished during a sabbatical stay at School of Geography and Oceanography, ADFA, University of New South Wales, Canberra, Australia, with support from ADFA, CONACYT and CICESE. The authors want to thank the enthusiastic support of the crew of the RV *Francisco de Ulloa*, and the field and cabinet efforts of Carlow Cabrera, Emilo Palacios and Salvador Sánchez.

References

Alvarez-Borrego, S., Galindo-Bect, L. A. & Flores-Báez, B. P. 1973 Hidrologia. En *Estudio Quimico Sobre la Contaminación por Insecticidas en la Desembocadura del Rio Colorado*. Tomo II. Reporte Final a la Dirección de Acuacultura de la Secretaria de Recursos Hidráulicos. Universidad Autónoma de Baja California. 248 pp.

Alvarez-Borrego, S. & Galindo-Bect, L. A. 1974 Hidrologia del Alto Golfo de California-I. Condiciones durante otoño. *Ciencias Marinas* **1**, 46–64.

Alvarez-Borrego, S., Flores-Báez, B. P. & Galindo-Bect, L. A. 1975 Hidrologia del Alto Golfo de California II. Condiciones durante invierno primavera y verano. *Ciencias Marinas* **2**, 21–36.

Alvarez-Borrego, S. & Schwartzlose, R. 1979 Water masses of the Gulf of California. *Ciencias Marinas* **6**, 43–63.

Alvarez Sánchez, L. G., Godínez, Victor. M., Lavín, M. F. & Sánchez, S. 1993 Patrones de turbidez y corrientes en la Bahia de San Felipe, al NW del Golfo de California. *Communicaciones Académicas CICESE*, CTOFT-9304, 48 pp.

Argote, M. L., Amador, A., Lavín, M. F. & Hunter, J. R. 1995 Tidal dissipation and stratification in the Gulf of California. *Journal of Geophysical Research* **100**, 16103–16118.

Argote, M. L. Lavín, M. F. & Amador, A. 1998 Barotropic residual circulation in the Gulf of California due to the M_2 tide and wind stress. *Atmósfera* (in press).

Beier, E. 1997 A numerical investigation of the annual variability in the Gulf of California. *Journal of Physical Oceanography* **27**, 615–632.

Bowden, K. F. & Fairbairn, L. A. 1952 A determination of the frictional forces in a tidal current. *Proceedings of the Royal Society of London, Series A* **214**, 371–392.

Bowers, D. G. & Lennon, G. W. 1987 Observations of stratified flow over a bottom gradient in a coastal sea. *Continental Shelf Research* **9**, 1105–1121.

Bowers, D. G. 1989 Models of density current outflows from inverse estuaries: with application to Spencer Gulf, South Australia. In *Focus on Modelling Marine Systems Vol. 2* (Davies, A. M., ed.). CRC State-of-the-art series on numerical Modelling of Marine Systems, pp. 1–23.

Bray, N. 1988 Water mass formation in the Gulf of California. *Journal of Geophysical Research* **93**, 9223–9240.

Carbajal, N. 1993 *Modelling of the Circulation in the Gulf of California*. PhD. thesis, Institute of Oceanography, University of Hamburg.

Carbajal, N., Souza, A. & Durazo, R. 1997 A numerical study of the ex-ROFI of the Colorado River. *Journal of Marine Systems* **12**, 17–33.

Castro, R., Lavín, M. F. & Ripa P. 1994 Seasonal heat balance in the Gulf of California. *Journal of Geophysical Research* **99**, 3249–3261.

de Silva Samarasinghe, J. R. & Lennon, G. W. 1987 Hypersalinity, flushing and transient salt-wedges in a tidal gulf-an inverse estuary. *Estuarine, Coastal and Shelf Science* **24**, 483–498.

de Silva Samarasinghe, J. R. 1989 Transient salt-wedges in a tidal gulf: a criterion for their formation. *Estuarine, Coastal and Shelf Science* **28**, 129–148.

García Córdoba, J., Róbles, J. M. & Flores Cabrera, C. F. 1995 Datos de CTD obtenidos en la Bahia de Todos Santos, B. C. Campaña BATOS 4. B/O Francisco de Ulloa. Marzo 22–24 de 1994. *Comunicaciones Académicas, Serie Oceanografia Fisica No. CTOFT9506*. CICESE, Ensenada, México. 75 pp.

Godínez, Victor. M., Lavín, M. F. & Sánchez Mancilla, S. 1995 Calibración del CTD Smart en laboratorio y campo. *Comunicaciones Académicas, Serie Oceanografia Fisica No. CTOFT9511*. CICESE, Ensenada, México. 14 pp.

Griffiths, R. W. 1986 Gravity currents in rotating systems. *Annual Review of Fluid Mechanics* **18**, 59–89.

Hunter, J. R. 1975 The determination of current velocities from diffusion/advection processes in the Irish Sea. *Estuarine and Coastal Marine Science* **3**, 34–55.

Lavín, M. F. & Organista, S. 1988 Surface heat flux in the Northern Gulf of California. *Journal of Geophysical Research* **93**, 14033–14038.

Lavín, M. F., Gaxiola Castro, G., Róbles, J. M. & Richter, K. 1995 Winter water masses and nutrients in the northern Gulf of California. *Journal of Geophysical Research* **100**, 8587–8605.

Lavín, M. F., Durazo, R., Palacios, E., Argote, M. L. & Carrillo, L. 1997 Lagrangian observations of the circulation in the Northern

Gulf of California. *Journal of Physical Oceanography* 27, 2298–2305.

Lennon, G. W., Bowers, D., Nunes, R. A., Scott, B. D., Ali, M., Boyle, J., Wenju, C., Hertzfeld, M., Johansson, G., Nield, S., Petrusevics, P., Stephenson, P., Suskin, A. A. & Wijffels, S. E. A. 1987 Gravity currents and the release of salt from an inverse estuary. *Nature* 327, 695–697.

Linden, P. F. & Simpson, J. E. 1986 Gravity-driven flows in a turbulent fluid. *Journal of Fluid Mechanics* 172, 481–497.

Linden, P. F. & Simpson, J. E. 1988 Modulated mixing and frontogenesis in shallow seas and estuaries. *Continental Shelf Research* 8, 1107–1127.

López, M. 1997 A numerical simulation of water mass formation in the northern Gulf of California during winter. *Continental Shelf Research* 17, 1581–1607.

Marinone, S. G. 1997 Tidal residual currents in the Gulf of California: is the M_2 tidal constituent sufficient to induce them? *Journal of Geophysical Research* 102, 8611–8623.

Martinez Sepúlveda, M. 1994 *Descripción de la Capa Mezclada Superficial del Golfo de California*. BSc thesis, Facultad de Ciencias Marinas, UABC, Ensenada, México. 48 pp.

Nunes Vaz, R. A. & Lennon, G. W. 1986 Physical property distributions and seasonal trends in Spencer Gulf, South Australia: an inverse estuary. *Australian Journal of Marine and Freshwater Research* 37, 39–59.

Nunes Vaz, R. A., Lennon, G. W. & de Silva Samarasinghe, J. R. 1989 The negative role of turbulence in estuarine mass transport. *Estuarine, Coastal and Shelf Science* 28, 361–377.

Nunes Vaz, R. A. & Lennon, G. W. 1987 Episodic stratification and gravity currents in a marine environment of modulated turbulence. *Journal of Geophysical Research* 92, 5465–5480.

Nunes Vaz, R. A. 1989 Periodic stratification in coastal waters. In *Modelling Marine Systems Volume 2*, (Davis, E. M., ed.). 69–105.

Nunes Vaz, R. A., Lennon, G. W. & Bowers, D. G. 1990 Physical behaviour of a large, negative or inverse estuary. *Continental Shelf Research* 10, 277–304.

Nunes Vaz, R. A. & Simpson, J. H. 1994 Turbulence closure modeling of estuarine stratification. *Journal of Geophysical Research* 99, 16143–16160.

Organista Sandoval, S. 1986 *Flujos de Calor en el Alto Golfo de California*. MSc thesis, CICESE, Ensenada, México. 142 pp.

Provis, D. G. & Lennon, G. W. 1983 Eddy viscosity and tidal cycles in a shallow sea. *Estuarine, Coastal and Shelf Science* 16, 351–361.

Reyes, A. C. & Lavin, M. F. 1997 Effects of the autumn-winter meteorology upon the surface heat loss in the Northern Gulf of California. *Atmósfera* 10, 101–123.

Robles, J. M. & Marinone, S. G. 1987 Seasonal and interannual hermohaline variability in the Guaymas basin in the Gulf of California. *Continental Shelf Research* 7, 715–733.

Romero Centeno, R. 1995 *Comportamiento de los Campos Hidrográficos y Flujos de Calor y Masa en el Canal de Ballenas*. MSc thesis, CICESE.

Simpson, J. E. 1982 Gravity currents in the laboratory, atmosphere, and ocean. *Annual Reviews of Fluid Mechanics* 14, 213–234.

Simpson, J. H., Brown, J., Matthews, J. P. & Allen, G. 1990 Tidal straining, density currents and stirring in the control of estuarine stratification. *Estuaries* 12, 125–132.

Sverdrup, H. U. 1941 The Gulf of California: preliminary discussion of the cruise of the *E. W. Scripps* in February and March 1939. *Proceedings of the 6th Pacific Science Conference*, pp. 161–166.

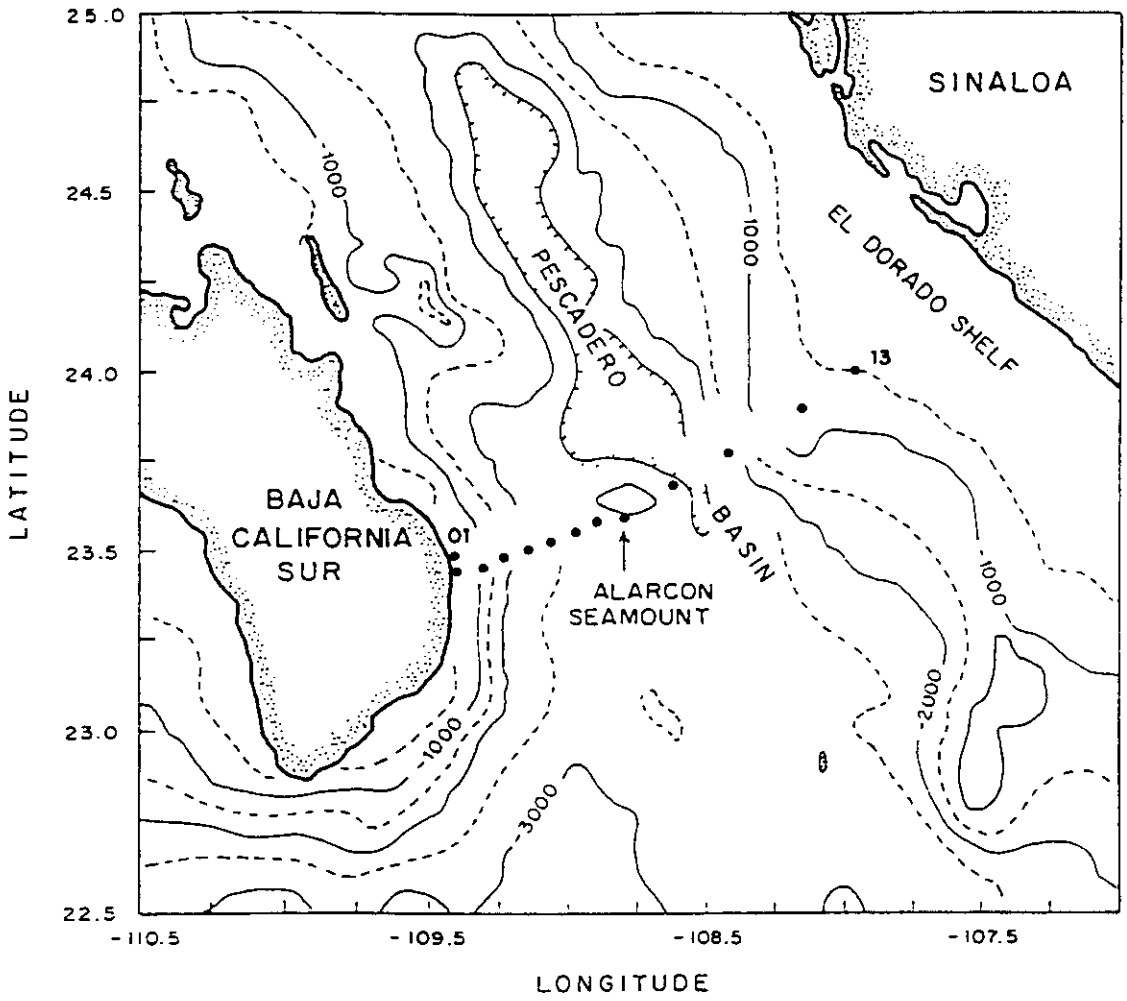

Flow into the Gulf of California.

Mascarenhas
Collins
Castro
Sánchez

Flow Into the Gulf

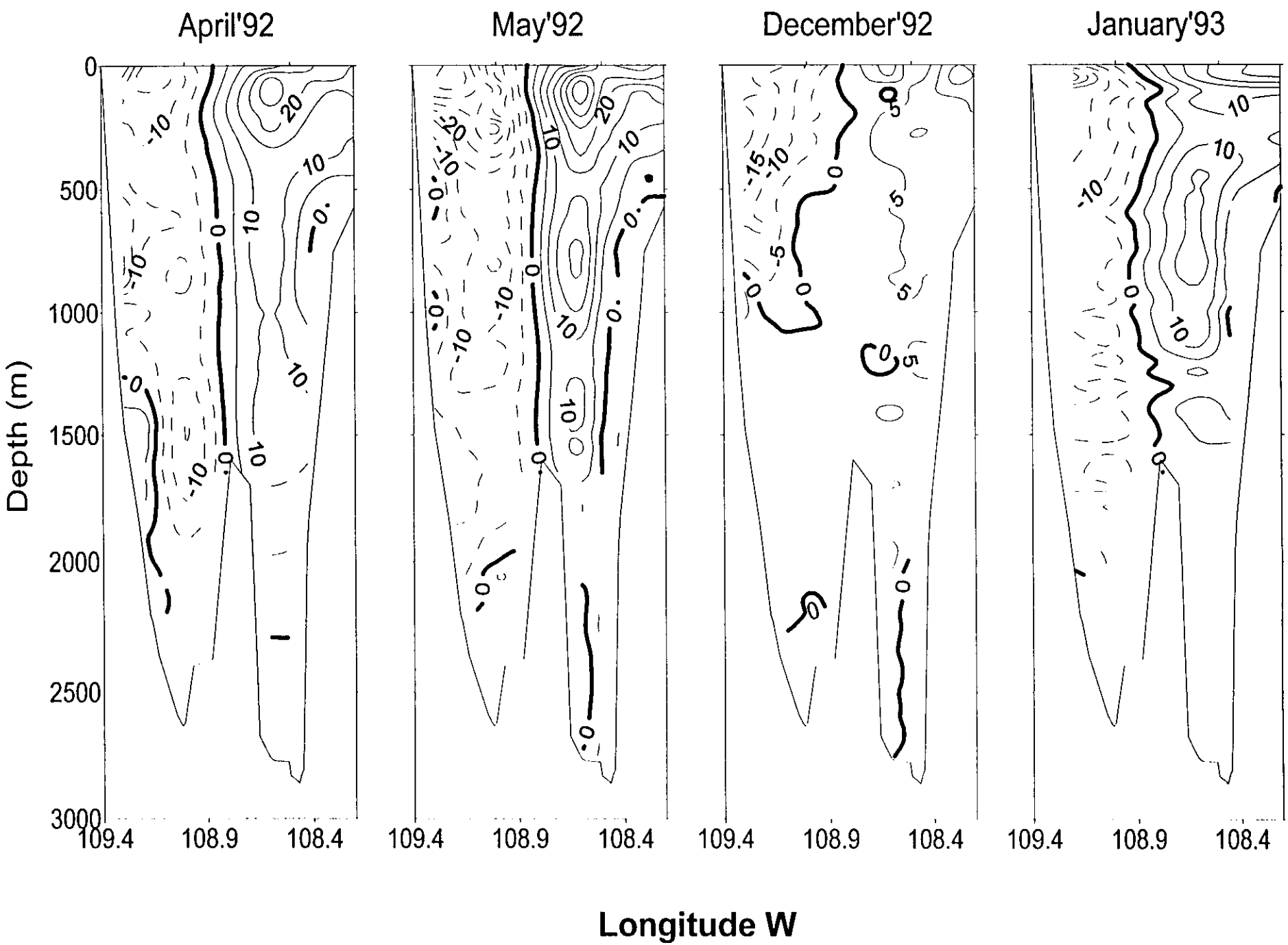

Conclusions

- There are gravity currents in the upper Gulf of California
- These occurr in summer and winter, on the western side
- They are intensified during neap tides
- In winter the gravity current reaches the bottom of the Wagner Basin (200 m), in summer a mid-depth (~ 40m) intrusion is produced.
- The suspended sediments concentration is highly correlated with the tidal current speed.

What causes the modulation of gravity currents by tides? (Do the high mixing during spring tides 'chokes' the gravity current?)

What is the role of gravity currents in:

a) the renewal of waters (ventilation)?
b) the heat and salt balances?
c) sediment transport (?, maybe, larvae)?